Draft version March 8, 2020
Typeset using LaTeX **twocolumn** style in AASTeX62

Dwarf Satellite Systems in the Local Volume: Cleaned Luminosity Functions and Host-to-Host Scatter

(Accepted March 8, 2020)

Submitted to ApJ

ABSTRACT

We measure the surface brightness fluctuation (SBF) distances to recently cataloged candidate dwarf satellites around 10 massive hosts in the Local ($D < 12$ Mpc) Volume (LV) to confirm association. The hosts are: NGC 1023, NGC 1156, NGC 2903, NGC 4258, NGC 4565, NGC 4631, NGC 5023, M51, M64, and M104. We are able to measure robust SBF distances for **xx** out of the **xx** candidates that had no previous distance information. We confirm a further **xx** candidates to be background from their lack of SBF. Using these results and any prior distance information, we argue that the satellite systems of these hosts are mostly cleaned of contaminants down to $M_g \sim -9$ to -10, depending on the host, and complete to that magnitude within the area of the search footprint. We consider the satellite systems of the six best surveyed hosts in more detail, along with the six nearby hosts that have been well-surveyed in the literature. Using this much expanded sample, we explore how well cosmological simulations combined with common abundance matching (AM) relations match the observed satellite luminosity functions. We find overall fair agreement with the models across the host mass range for AM relations that agree well with state-of-the-art hydrodynamic simulations. Critically, we find that the host-to-host scatter predicted by the model is in close agreement with the scatter between the observed systems, once the different masses of the observed systems are taken into account. However, we do find that the observed systems have more bright and fewer faint satellites than the AM model predicts. We provide tables of the properties of all the satellites systems considered here for use in future explorations of small scale structure.

Keywords: methods: observational – techniques: photometric – galaxies: distances and redshifts – galaxies: dwarf

1. INTRODUCTION

For over two decades, the satellites of the Milky Way (MW) have been an important testing ground for the ΛCDM model of structure formation. Within the last few years, hydrodynamic simulations have gotten to the resolution required to resolve the formation of the bright MW 'classical' ($M_* \gtrsim 10^5 M_\odot$) satellites. Results from the APOSTLE (Sawala et al. 2016a), FIRE (Wetzel et al. 2016; Garrison-Kimmel et al. 2019), and NIHAO (Buck et al. 2019) projects show that the inclusion of baryonic physics leads to simulated satellite systems that have similar satellite numbers and internal kinematics compared with the MW and M31 systems. These results suggest resolutions to the long-standing 'Missing Satellites' (Klypin et al. 1999; Moore et al. 1999) and 'Too Big to Fail' Problems (Boylan-Kolchin et al. 2011, 2012) associated with dissipationless dark matter only (DMO) simulations of structure formation.

However, as observations and simulations improve, more mysteries and possible tensions with ΛCDM have been uncovered. Results from the *Gaia* mission have shown with ever-improving precision that most of the classical satellites of the MW lie in a rotationally supported disk (Fritz et al. 2018). The occurrence of such structures is exceedingly rare in ΛCDM simulations of structure formation (Pawlowski et al. 2012; Pawlowski & Kroupa 2013; Pawlowski 2018; Pawlowski & Kroupa 2019). Similar, but less well-characterized, structures have been found around M31 and Centaurus A (Ibata et al. 2013; Müller et al. 2018b). These structure are also outliers in ΛCDM simulations (Cautun et al. 2015). Additionally, the radial distribution of MW satellites

Corresponding author: Scott G. Carlsten
scottgc@princeton.edu

appears to be more centrally concentrated than ΛCDM simulations, both among the classical satellites (Yniguez et al. 2014; Samuel et al. 2020) and ultra-faints (Graus et al. 2019).

Furthermore, early observational results have suggested that the host-to-host scatter between satellite systems of nearby MW-analogs is larger than that expected in ΛCDM simulations. The SAGA Survey (Geha et al. 2017) characterized the bright ($M_r < -12.3$) satellites of 8 nearby MW-analogs and noted that the scatter in satellite richness between hosts appeared to be larger than that predicted from abundance matching (AM) applied to DMO simulations. Smercina et al. (2018) conducted a deep survey of the classical satellites of M94 and found only two satellites with $M_V < -9$ in the inner projected 150 kpc volume. This is to be contrasted with the 7 (LMC, SMC, Sgr, Fornax, Sculptor, Sextans, and Carina) such satellites within 150 kpc of the MW. They argue that common AM relations used with the DMO results from the EAGLE Project (Schaye et al. 2015) predict far too little scatter to explain M94's anemic satellite population. They suggest that significantly increasing the scatter in the stellar-halo mass relation (SHMR) could explain M94's satellite system.

The motivation to study dwarf satellite systems outside of the MW is thus twofold. First, the satellite systems of MW-analogs are necessary to quantify the host-to-host scatter which is an important benchmark to compare with simulations and an indicator of how stochastic galaxy formation is on these small scales. Second, the satellite systems of nearby hosts can tell us if and how satellite property and abundance changes with host property, like host mass, environment, morphology, and accretion history. Once the MW's satellite system is put into such a cosmological context, hopefully some explanation can be found for some of the outstanding questions raised above.

Much work has been done in this area in the last few years from several groups, but due to the difficult nature of finding and confirming low mass companions around massive hosts in the Local Volume (LV), only a handful of hosts have been surveyed at a level comparable to the classical satellites of the MW. The PAndAS Project (McConnachie et al. 2009; Martin et al. 2016; McConnachie et al. 2018) has surveyed most of the virial volume of M31 for satellites and halo substructure. Chiboucas et al. (2009) and Chiboucas et al. (2013) have surveyed the virial volume of M81 for satellites, uncovering a rich system. Centaurus A has been surveyed by multiple groups including Crnojević et al. (2014, 2019) and Müller et al. (2017, 2015, 2019). As mentioned above, Smercina et al. (2018) surveyed the M94 system. Finally, M101 has been well surveyed by the combined effort of Danieli et al. (2017); Bennet et al. (2017); Carlsten et al. (2019a); Bennet et al. (2019). Thus only 6 roughly MW-like, nearby systems have been surveyed with significant completeness.

A significant part of the difficulty of this endeavor is in measuring the distances to candidate satellites and confirming their association with the massive host. Many more hosts have been surveyed and candidate satellites have been found around, for instance: Leo I (Müller et al. 2018a), NGC 2784 (Park et al. 2017), NGC 4258 (Kim et al. 2011), NGC 3585 (Park et al. 2019), NGC 1291 (Byun et al. 2020), amongst others. For the systems that have had their satellites confirmed with distance measurements, the contamination of unrelated background galaxies can be quite high. Carlsten et al. (2019a) and Bennet et al. (2019) found that the contamination fraction of the candidate satellite catalog of Bennet et al. (2017) for M101 was ∼80%**calculate**. This added scatter will obfuscate the interpretation of host-to-host scatter in satellite number. While some of this can be overcome by careful statistical subtraction of a background luminosity function (LF), in this work, we opt for the safer route of only considering the satellite systems which have been fully confirmed with distance measurements.

For distance measurements, TRGB measurements with *HST* are usually used. Due to the small FOV of *HST*, these measurements can be quite expensive, requiring many orbits to measure the distances to a large number of candidates. An alternative is to measure the distances with surface brightness fluctuations (SBF) from the ground. SBF has been shown to be a very efficient distance measure for low surface brightness (LSB) dwarfs (e.g. Jerjen et al. 1998, 2000, 2001; Jerjen 2003; Jerjen et al. 2004; Mieske et al. 2007, 2006; Carlsten et al. 2019b). Carlsten et al. (2019b) derived an absolute calibration in the i band based solely on TRGB distances and found that SBF distances could reproduce the TRGB distances with ∼15% accuracy, even for $\mu_0 \sim 26$ mag arcsec^{-2} dwarfs.

The goal of the current paper is two-fold: First, we measure the distance via SBF for a large number of candidate satellites found in the recent search around 10 LV hosts of Carlsten et al. (2019c). We will use the same ground-based data that was used to detect the candidates. While we primarily use SBF as a distance indicator, we use redshifts and TRGB distances, where available. Since several of the hosts had r band imaging and not i or had significantly deeper r band imaging, we derive an absolute SBF calibration for the r band in this paper as well. Many previous calibrations (including that of Carlsten et al. (2019b)) are for the i band. While SBF is less prominent in bluer bands (Jensen et al. 2003) and seeing is generally worse (Carlsten et al. 2018), robust SBF distances are still possible in the r band. Second, we explore the luminosity functions of the cleaned satellite systems together with the previously known systems. We explore how well AM relations together with modern cosmological simulations can reproduce the observed LFs, including the host-to-host scatter.

This paper is structured as follows: in §2 we describe the candidate sample and data reduction, in §3 we outline the SBF methodology used, in §4 we derive an absolute SBF calibration for the r band, in §5 we present our distance results, and in §6 we discuss the cleaned samples of satellites. In §7, we collate all of the satellite systems currently surveyed in the LV and compare their luminosity functions. In §8 we introduce the simulations and models that we use to compare with the data, in §9 we discuss the results of the comparison, and, finally, we conclude in §10. Readers interested primarily in the analysis of the satellite systems and comparison with models can skip to §6.

2. DATA

We base this paper on the catalog of candidate satellites of Carlsten et al. (2019c). Carlsten et al. (2019c) searched for candidates satellites around 10 massive primaries in the LV using wide-field deep archival CFHT/MegaCam imaging. The surveyed hosts are: NGC 1023, NGC 1156, NGC 2903, NGC 4258, NGC 4565, NGC 4631, NGC 5023, M51, M64, and M104. The area and surface brightness completeness were heterogeneous but several of the hosts were nearly completely surveyed within a projected radius of 150 kpc down to $\mu_{g,0}{\sim}26$ mag arcsec^{-2}. These completeness levels were determined by careful mock galaxy tests.

In this paper, we use the same archival CFHT/MegaCam (Boulade et al. 2003) imaging data as used by Carlsten et al. (2019c). Either g and r or g and i band imaging is used, depending on the availability in the CFHT archive. Exposure times are characteristically ∼1 hour in each of the bands. The data reduction follows that in Carlsten et al. (2019c) and we refer the reader there for details.

Carlsten et al. (2019c) used the object detection algorithm of Greco et al. (2018) which is specifically optimized for LSB galaxies and detected xx candidate satellite galaxies around these hosts. While the detection algorithm focused on LSB galaxies, Carlsten et al. (2019c) cataloged many HSB candidates in the regions as well. We use the catalogs of Carlsten et al. (2019c) as the basis for the SBF analysis presented here. While most of the cataloged galaxies have no prior distance information, some have redshifts and some even have TRGB distances. Where possible, we take these into account when confirming or not a candidate as a real satellite. We refer the reader to Carlsten et al. (2019c) for the full catalogs of candidates.

3. SBF METHODOLOGY

In this section, we describe the methodology we use in the SBF analysis. We mostly follow the procedure detailed in Carlsten et al. (2019b) which largely follows the usual SBF measurement process (e.g. Blakeslee et al. 2009; Cantiello et al. 2018). We briefly outline the important steps here. The analysis starts with the rereduced cutouts for each detected dwarf. We use the Sérsic fits reported by Carlsten et al. (2019c) as the model for the smooth galaxy profile in the SBF measurement. This is non-ideal for many of the galaxies which do not appear to be well modelled by a Sérsic profile but, unfortunately, it is necessary as most of the galaxies are too faint and/or small for any sort of non-parametric profile to be fit. Using a Sérsic profile as a model for the smooth underlying galaxy profile where, in reality, the galaxy profile is more complicated can lead to spurious fluctuation power in the SBF measurement and can bias the distance significantly. To overcome this, for a small sub-sample of the galaxies, we redo the Sérsic fits and restrict the fits only to the outer regions of the galaxies, which are often smoother and more amenable to SBF. The color inferred from these fits, and not the fits from Carlsten et al. (2019c), are used in the SBF analysis, but the photometry from Carlsten et al. (2019c) is used in all of the luminosity function analysis.

The Sérsic profiles are subtracted from the images and the images are normalized by the square root of the profile. The images are masked for foreground MW stars and background galaxies (and possibly star clusters in the dwarf being analyzed) that can contribute spurious fluctuation power in the SBF measurement. Determining the threshold at which to mask contaminating point sources requires some care as it is important to mask as much contaminants as possible but not mask any of the peaks in the SBF. To determine the threshold, we calculate what pixel intensity would correspond to a point source with absolute magnitude ~ -5 at the distance of the host around which the dwarf is found. This is converted into a number of standard deviations above the background and the images are masked down to this level. A threshold of $M \sim -5$ mag will mask almost any globular cluster associated with the dwarf but still leave the red giant stars that are creating the SBF unmasked.

This threshold is tweaked a little on a per-galaxy bias to make sure that clear contaminants get masked.

For each galaxy, an annulus is chosen within which the Fourier transform is taken and the power spectrum of the image is calculated. For most LSB dwarfs the annulus is the region where the smooth galaxy model is > 0.4 times its peak value. This is found to roughly maximize the signal to noise of the SBF measurement. For the galaxies where the Sérsic profile does not appear to represent the galaxy well, often the annulus is chosen to cover the outer envelope of the galaxy which are often much better represented by the Sérsic profile than the inner regions. The power spectra are azimuthally averaged and are fit with a linear combination of a constant (which represents the contribution from white photometric noise) and the 'expectation power spectrum' which is a convolution of the PSF power spectrum and the mask power spectrum. The SBF level is given by the coefficient of the expectation power spectrum in the best fit. The PSF at the location of each dwarf is modeled from a cutout of a single bright, unsaturated star that is near to the dwarf's location. Choosing different stars for the PSF model does affect the measured SBF level but at a level $\lesssim 0.1$ mag which is generally less than other sources of uncertainty and so we do not include it in the error budget.

To deal with residual contaminant sources that are below the masking threshold and also the spurious power coming from the fact that the photometric noise is not white due to the resampling that occurs in the coaddition process, we measure the SBF variance in nearby empty fields that are masked and normalized in the same way as the real galaxy. This residual SBF level is subtracted off from that of the galaxy. To estimate the uncertainty in the SBF measurement, we do a Monte Carlo approach where for each iteration, we fit the power spectrum over a different range in wavenumber and we choose a different nearby background field to model the residual SBF level. We use the median of the resulting distribution as the measured SBF variance level and the spread as the uncertainty.

The main steps in the SBF measurement are shown in Figure 1 for six example dwarfs in our catalog. Many of the dwarfs are LSB with $\mu_{0,g}{\sim}26$ mag arcsec^{-2} but high S/N SBF measurements are still possible with the depth of the archival data.

To turn the SBF measurement into a distance constraint, we use the calibration of Carlsten et al. (2019b). This calibration accounts for the dependence of SBF on stellar population via the integrated $g - i$ color of a galaxy. It provides the absolute SBF magnitude in the i-band. However, for seven of our hosts, our imaging data is in the g and r-bands, not g and i. In §4 below we extend the calibration of Carlsten et al. (2019b) into the r-band using simple stellar population isochrone models and the subsample of calibrator galaxies of Carlsten et al. (2019b) that have r-band imaging data. This calibration models the absolute r-band SBF magnitude as a function of integrated $g - r$ color. Using either calibration, we follow the same procedure to turn the SBF measurement into a distance constraint. Here, again, we use a Monte Carlo approach. For each iteration, we sample a color from a Gaussian with mean equal to the measured color of the galaxy and standard deviation equal to the estimated uncertainty in the color. With this color we use an SBF calibration to derive an absolute SBF magnitude. To account for the uncertainties in the calibration, in each iteration, we sample the calibration parameters from the Markov Chain Monte Carlo chains. This accounts for the strong covariance between the slope and y-intercept in the calibration formula. Finally, in each iteration, we sample an SBF level from a Gaussian with mean equal to the measured SBF variance and standard deviation equal to the estimated uncertainty in the SBF variance. From this and the absolute SBF magnitude, we derive a distance. After doing all the Monte Carlo iterations, we are left with a distribution in distances that are consistent with the measured SBF and color for a galaxy. From this distribution, we calculate a median distance and $\pm 1\sigma$ and $\pm 2\sigma$ distance bounds.

For many of the candidate dwarf sample, the measured SBF level is very low and it is possible to show that these must be background galaxies. Following Carlsten et al. (2019a), we consider any dwarf whose 2σ distance lower bound is beyond the distance of the host to be background. It is important to note that this is not simply a statement of the signal to noise of the SBF measurement. Additionally, concluding galaxies are background is not simply due to the galaxies being too faint to measure SBF. The uncertainty of the SBF measurement is used in the distance constraint and thus the faintness of the galaxy is accounted for. Concluding that galaxies are background is essentially a statement that the measured SBF variance is $> 2\sigma$ below what would be expected for a galaxy of a certain color at the distance of the host. Carlsten et al. (2019a) concluded that many candidate satellites of M101 were background and this has since been confirmed by HST imaging (Bennet et al. 2019), demonstrating that SBF distance lower bounds set in this way are legitimate.

Some of the galaxies that we confirm to be background appear to have relatively tight distance errorbars around some distance behind the host galaxy. We emphasize

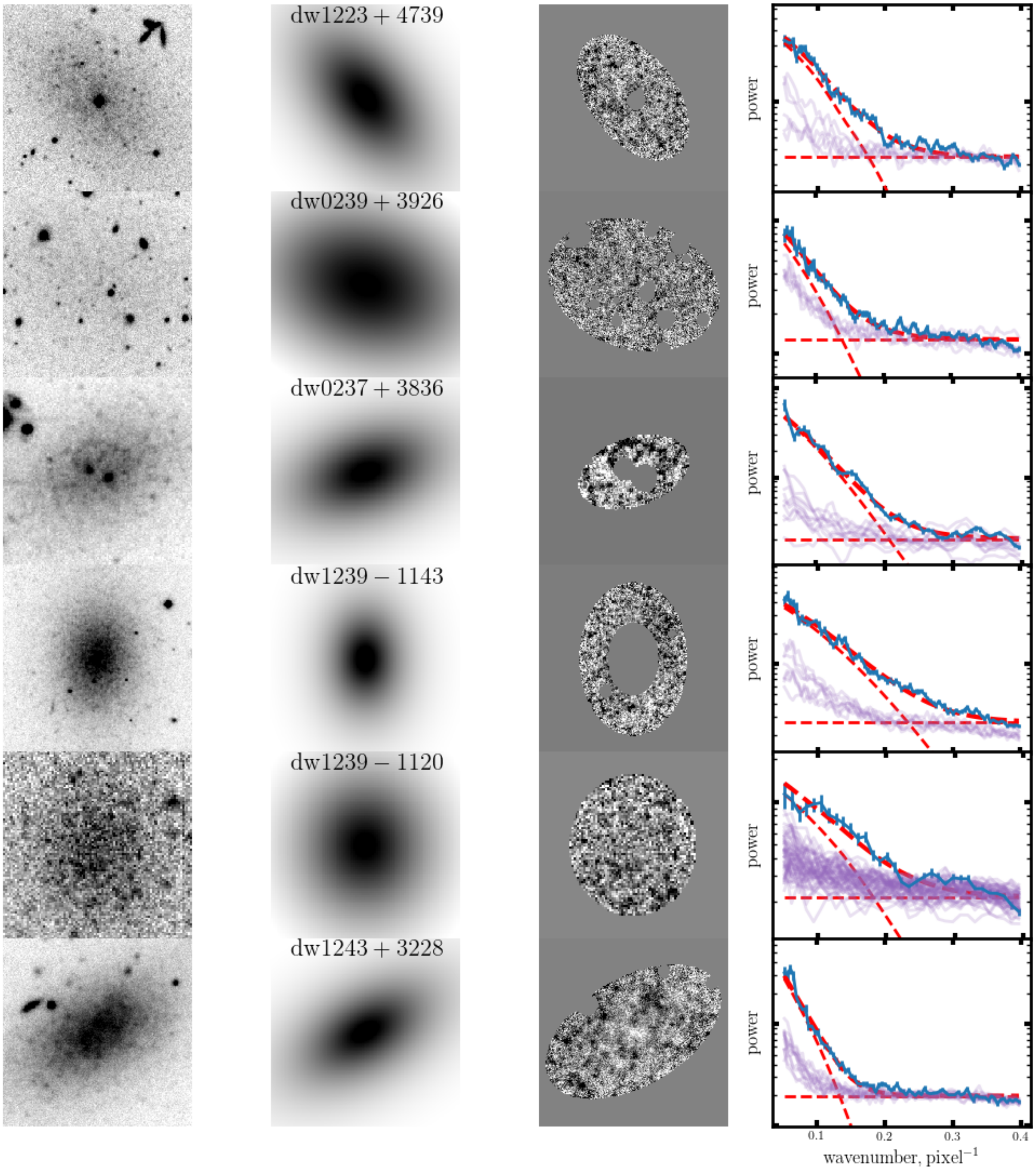

Figure 1. Demonstration of the SBF measurement process. The stacked r or i band images of the dwarfs are shown in the left column. The Sérsic fit used to model the smooth galaxy profile is shown in the second column. This smooth model is subtracted from the galaxy and used to normalize the galaxy. Any contaminating point sources are masked and an annulus is chosen within which to measure the SBF. This result is shown in the third column. The azimuthally averaged power spectrum is shown in the right column along with the fitted combination of PSF power spectrum and white noise (the units are arbitrary). The faint purple lines are the power spectrum measured in the background fields. Note that even though dw0239+3926 is very LSB, a high S/N∼15 measure of the SBF is possible.

that these should generally not be trusted. The fluctuation signal that is driving the tight distance constraint is more often than not coming from residuals due to assuming a Sérsic profile when the galaxy profile is actually more complicated and not real SBF. The conclusion that these galaxies are background is, however, solid because even with this added fluctuation power, the galaxies do not show the fluctuations that would be expected for a galaxy at the distance of the host.

Examples of galaxies that we conclude to be background along with examples of galaxies that we conclude to be real satellites from the same host are shown in Appendix E.

4. r BAND SBF CALIBRATION

Carlsten et al. (2019b) provide a calibration for $\bar{M}_i$ as a function of $g-i$ color, however, many of our host galaxies only have imaging in r or the r coverage is significantly more than the i-band. In this section, we extend the work of Carlsten et al. (2019b) and provide a calibration for $\bar{M}_r$ as a function of $g-r$ color. Many of the galaxies used in the calibration of Carlsten et al. (2019b) have r-band data and it is possible to measure the r-band SBF magnitudes for these galaxies. There are 12 galaxies in the calibration sample with r-band imaging. We supplement this sample with two additional dwarf satellites in the M81 group that have CFHT g and r imaging and HST TRGB (Chiboucas et al. 2009, 2013). These 14 galaxies are listed in Table 4 (we refer the reader to Carlsten et al. (2019b) for more details on these galaxies).

Table 1. Galaxies used in the r band Calibration

Name	Distance (Mpc)
FM1	3.78
KDG 061	3.66
BK5N	3.7
UGCA 365	5.42
DDO 044	3.21
d0939+71	3.7
d0944+71	3.4
LVJ1218+4655	8.28
NGC 4258-DF6	7.3
KDG 101	7.28
M101-DF1	6.37
M101-DF2	6.87
M101-DF3	6.52
UGC 9405	6.3

Do to the significantly lower number of calibration galaxies available for the r-band than the i-band, we opt to not simply fit a $\bar{M}_r$ vs $g-r$ calibration but instead convert the $\bar{M}_i$ vs $g-i$ calibration into the r band using theoretical isochrones and show that it is consistent with the SBF observations of the galaxies in Table 4. The uncertainties associated with the filter transform are likely smaller than the uncertainties that will come from fitting the small number of available calibrator galaxies. Carlsten et al. (2019b) found only modest agreement with the theoretical $\bar{M}_i$ vs $g-i$ relation predicted by either the MIST (Choi et al. 2016) or PADOVA (Bressan et al. 2012; Marigo et al. 2017) isochrone models. In that work, it was unclear whether the disagreement (especially prominent at bluer colors) was due to the models or the SBF measurements. However, we are not using the isochrones to provide an absolute r-band calibration but convert the empirical i-band calibration into the r-band which we believe will be much more reliable.

To do this conversion, we derive $\bar{M}_i$ to $\bar{M}_r$ and $g-i$ to $g-r$ conversions using SSP models from the MIST project with ages between 3 and 10 Gyr and metallicities in the range $-2 < \mathrm{[Fe/H]} < 0$. Both conversions are fit as linear functions of the $g-r$ color. These conversions are shown in Appendix D. The $\bar{M}_i$ to $\bar{M}_r$ conversion is fit only in the color range $g-r < 0.6$ which is appropriate for the low mass galaxies we use this calibration for in this paper.

With conversion functions of the form:

$$\begin{aligned} \bar{M}_i - \bar{M}_r &= a(g-r) + b \\ (g-r) - (g-i) &= a_2(g-r) + b_2 \end{aligned} \tag{1}$$

and an i-band calibration of the form:

$$\bar{M}_i = \alpha(g-i) + \beta, \tag{2}$$

the r-band calibration can be written as:

$$\bar{M}_r = (\alpha - a - \alpha a_2)(g-r) - b - \alpha b_2 + \beta. \tag{3}$$

Doing the fits, we find $a = -0.92$, $b = -0.243$, $a_2 = -0.530$, and $b_2 = 0.0319$ which yields the calibration (using α/β from Carlsten et al. (2019b)):

$$\bar{M}_r = 4.21(g-r) - 3.00. \tag{4}$$

To calculate distance uncertainties when using this calibration, we sample from the chains in the MCMC fit of Carlsten et al. (2019b) and convert those into uncertainties in $\bar{M}_r$ using Equation 3 above. Using the chains is

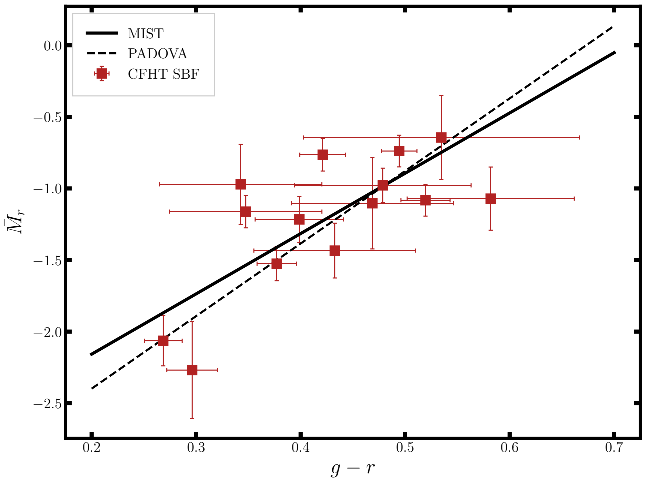

Figure 2. The SBF r-band calibration used in this work. The black lines show the i-band calibration of Carlsten et al. (2019b) converted into the r-band using theoretical isochrones. The points are CFHT SBF measurements of galaxies with known TRGB distances.

crucial to capture the covariance between the slope and y-intercept in the calibration.

The calibration in Equation 4 is shown in Figure 2 along with the 14 calibrator galaxies. The agreement in the color range $0.3 < g - r < 0.6$ is quite good between the observations and the converted i-band calibration. We calculate a reduced χ^2 (e.g. Eq 5 of Carlsten et al. (2019b)) of the data points relative to the MIST line of $\chi^2_{\rm red}$=2.0, indicating the agreement is acceptable. We take this as evidence that the systematic uncertainties involved in the filter transform are minimal. Also shown in the dashed line is the calibration that results from using PADOVA isochrones instead of MIST isochrones. We see that the difference is minimal in the color range $0.3 < g - r < 0.6$ which is where most of the galaxies that we use this formula for are.

5. SBF DISTANCES

In this section, we go through each host and discuss the results of the SBF analysis. We split the dwarfs into three categories: confirmed physical satellites, confirmed background contaminants, or galaxies where no SBF constraint is possible. This last category is generally for galaxies that were so faint that the uncertainty in the SBF measurement is so great that they could essentially be at any distance. Additionally, some galaxies that were too extremely non-Sérsic or had other problems (for instance, being behind a saturation spike) that made the SBF measurement impossible are conservatively put into this category. Generally, we label a dwarf to be a confirmed satellite if the SBF is measured at a S/N > 5 and the distance is within $\sim 2\sigma$ of the host's distance. We define the SBF S/N as simply the measured SBF variance level divided by its estimated uncertainty. This cutoff in S/N is motivated from our experience that SBF becomes visually noticeable at around this S/N. A visual sanity check is important to make sure that the SBF signal is coming from bulk stellar population of the galaxy and not from star clusters or twists or other irregularities in the light profile. There are a few cases where we measure a high (> 5) S/N signal but conservatively include the galaxy into the 'undetermined' category because visually the fluctuation signal does not appear to be coming from the bulk stellar population of the galaxy.

Carlsten et al. (2019a) confirmed two satellites around M101 using SBF. These satellites had SBF S/N of ≥ 7 which means they would be confirmed by the threshold we use here. Both of these have been confirmed by the *HST* imaging of Bennet et al. (2019). Carlsten et al. (2019a) also highlighted 2 other candidates as promising follow-up targets that had reasonably strong signal (S/N$\sim$ $2-3$) but the *HST* imaging of Bennet et al. (2019) showed that this signal was not from SBF and the galaxies were background contaminants. We believe that the higher threshold we use here is conservative enough to prevent false positive satellite confirmation.

Galaxies whose distance is consistent with the host's distance but the SBF is of low significance (S/N < 5) are included in the 'unconfirmed' category. There are a few exceptions to these rules that we mention below. Where available, we also incorporate TRGB distances and redshifts into the confirmation or disconfirmation of satellites.

A summary of the SBF results are listed in Table 2. Here we list how many candidates are confirmed as satellites for each host, along with the number of confirmed background contaminants and the number of candidates that remain unconfirmed. In this table, we give the number of candidates confirmed via any method (including TRGB and/or redshift), although the vast majority are confirmed via SBF.

The main results of the SBF analysis are given in Tables 3-12. In these tables, we only list the galaxy name and the SBF results. More information, including photometry can be found in Carlsten et al. (2019c). For convenience, we include the photometry for the confirmed and possible satellites in Appendix A. Physical sizes and absolute magnitudes are included in those tables. In the following sub-sections, we go through each host and discuss the SBF results.

there are two maybes that have HST imaging... inspect more closely, n4631 and m51's blob

Table 2. Overview of the SBF results for each host.

Host Name	Host Distance (Mpc)	Host M_K	# Confirmed	# Possible	# Background
NGC 1023	10.4	-23.9	15	6	10
NGC 1156	7.6	-19.9	0	2	1
NGC 2903	8.0	-23.5	2	2	0
NGC 4258	7.2	-23.8	7	4	22
NGC 4565	11.9	-24.3	4	16	1
NGC 4631	7.4	-22.9	9	1	6
NGC 5023	6.5	-19.3	0	1	1
M51	8.6	-24.2	1	6	8
M64	5.3	-23.3	0	0	1
M104	9.55	-24.9	12	12	3

5.1. *NGC 1023*

Table 3 gives the SBF results for candidate satellites in the field of NGC 1023. Overall the SBF results are quite promising. Several of the dwarfs had very strong SBF signals that put them at the distance of NGC 1023 ($D = 10.4$ Mpc). For **four** of the candidates, we did not attempt an SBF measurement either because the candidate was too irregular or because there was too much scattered light from a nearby star. For three of these **IC 239, UGC 2157, and dw0240+3903**, the candidates have redshifts from Trentham & Tully (2009) that are within $\pm$300 km/s of NGC 1023. Trentham & Tully (2009) consider these three to be high confidence members for the NGC 1023 group, and we consider these to be confirmed members as well. All three have visible SBF that looks similar to other confirmed members of similar color. There were **two** objects **dw0237p3855 and dw0241p3904** which had very strong (S/N$\gtrsim$ 20) SBF signals but distances that were slightly inconsistent with NGC 1023. As discussed in Carlsten et al. (2019c), NGC 1023 has lots of contamination from scattered light from bright stars due to its low galactic latitude. **Both** of these objects were heavily contaminated by scattered light which is likely causing the discrepant distances. Both objects had visually similar SBF to other confirmed objects, and we consider it very likely that both are genuine members of the group. We note that there are a few candidates that we consider to be background with strong SBF signal and 2σ distance lower bounds only slightly beyond NGC 1023 (e.g. **dw0236p3752**). These galaxies do not suffer from the same amount of contamination as the confirmed candidates with discrepant distances, and there is no reason to believe the SBF distance is wrong in these cases.

5.2. *NGC 1156*

The SBF results for NGC 1156 are shown in Table 4. The SBF results for this region were very uncertain, largely due to the shallow data and significant contamination from galactic cirrus. We do not confirm any of the candidates to be genuine satellites. One of the candidates is likely background, and the other two are possible satellites. **One** of the possible satellites (dw0300p2514) was above our fiducial S/N> 5 threshold and had distance consistent with NGC 1156, but due to the galactic cirrus, we could not visually confirm this signal was actual SBF. Thus, we conservatively include this galaxy into the unconfirmed/possible satellite category. **dw0300p2514 and dw0301p2446** are the two objects cataloged by Karachentsev et al. (2015) and are both promising targets for follow-up.

5.3. *NGC 2903*

Table 5 lists the SBF results for NGC 2903. We confirm two candidates as satellites and leave two more as possible/unconfirmed satellites. Our SBF distance of UGC 5086 is likely quite trustworthy given the smooth, round morphology of that galaxy. The other confirmed satellite, dw0930+2143, is bluer, more irregular, and HI-rich (Irwin et al. 2009) so the SBF distance is more uncertain. Irwin et al. (2009) measured a redshift for this dwarf via HI observations that is quite close to that of NGC 2903 ($\Delta cz \sim 30$ km/s). Given the redshift and the fact that the SBF distance is consistent with that of NGC 2903, we consider this dwarf a likely genuine satellite.

5.4. *NGC 4258*

As shown in Table 6, the results for NGC 4258 are quite promising. Many candidates are shown to be background while only a few were inconclusive. Seven satellites are confirmed with the SBF. Four of these have TRGB distances that put them at the distance of

Table 3. NGC 1023 SBF Results

Confirmed			Possible			Background		
Name	SBF S/N	Dist (Mpc)	Name	SBF S/N	Dist (Mpc)	Name	SBF S/N	Dist (Mpc)
dw0233+3852	5.1	$12.1^{+2.1,4.7}_{-1.6,3.1}$	dw0238+3805	–	–	dw0234+3800	4.4	> 17.1
dw0235+3850	11.4	$11.6^{+0.9,1.9}_{-0.9,1.8}$	dw0239+3910	2.1	$12.0^{+5.1,\infty}_{-2.7,4.6}$	dw0236+3752	6.0	> 11.8
IC 239	–	–	dw0241+3852	1.9	$16.1^{+7.4,\infty}_{-3.7,6.1}$	dw0236+3925	1.4	> 13.8
dw0237+3855*	23.8	$7.1^{+0.5,1.0}_{-0.5,1.1}$	dw0241+3829	1.8	$12.6^{+6.1,\infty}_{-2.5,4.0}$	dw0237+3903	2.1	> 13.6
dw0237+3836	22.1	$10.5^{+0.8,1.6}_{-0.8,1.7}$	dw0242+3757	0.5	$13.2^{+\infty,\infty}_{-5.7,7.6}$	dw0238+3808	-0.7	> 17.5
dw0239+3926	15.3	$10.9^{+0.7,1.4}_{-0.7,1.5}$	dw0243+3915	1.2	$13.5^{+\infty,\infty}_{-3.6,5.5}$	dw0239+3824	0.7	> 12.5
dw0239+3903	9.5	$8.4^{+1.7,3.8}_{-1.5,2.8}$				dw0240+3844	5.9	> 16.6
dw0239+3902	7.1	$11.5^{+1.2,2.6}_{-1.1,2.1}$				dw0240+3829	-0.3	> 24.1
UGC 2157	–	–				dw0241+3923	0.4	> 16.3
dw0240+3854	18.4	$11.2^{+0.5,1.0}_{-0.5,0.9}$				dw0241+3934	1.6	> 13.0
dw0240+3903	–	–						
dw0240+3922	6.5	$11.7^{+1.2,2.8}_{-1.0,1.8}$						
dw0241+3904*	18.3	$11.9^{+0.5,1.1}_{-0.5,1.0}$						
UGC 2165	46.5	$10.8^{+0.8,1.6}_{-0.8,1.7}$						
dw0242+3838	5.9	$8.9^{+1.1,2.3}_{-0.9,1.6}$						

Note—SBF results for candidates around NGC 1023 ($D = 10.4$ Mpc). Objects are ordered as confirmed satellites, then possible (still unconfirmed) satellites, and then confirmed background contaminants. The SBF distances give $+1\sigma, +2\sigma$ errors in superscipt and $-1\sigma, -2\sigma$ errors in subscript. Lower distance limits (2σ) are given for the background objects. Objects with dashes through the measurements were too irregular and no SBF measurement was attempted. The objects that are confirmed without SBF measurements have redshifts. Objects with asterisks (*) are exceptions to the confirmation criteria outlined in §5, see text for details.

Table 4. NGC 1156 SBF Results

Confirmed			Possible			Background		
Name	SBF S/N	Dist (Mpc)	Name	SBF S/N	Dist (Mpc)	Name	SBF S/N	Dist (Mpc)
			dw0300+2514*	5.2	$8.0^{+2.2,5.1}_{-1.7,3.0}$	dw0300+2518	1.0	> 10.1
			dw0301+2446	4.6	$4.6^{+2.5,6.2}_{-1.6,2.7}$			

Note—Same as Table 3 for NGC 1156 ($D = 7.6$ Mpc).

Table 5. NGC 2903 SBF Results

Confirmed			Possible			Background		
Name	SBF S/N	Dist (Mpc)	Name	SBF S/N	Dist (Mpc)	Name	SBF S/N	Dist (Mpc)
dw0930+2143	6.0	$8.6^{+1.0,2.3}_{-0.8,1.5}$	dw0933+2114	1.5	$6.6^{+4.8,\infty}_{-1.9,3.2}$			
UGC 5086	9.6	$9.1^{+0.9,1.9}_{-0.9,1.8}$	dw0934+2204	2.6	$8.3^{+2.9,8.9}_{-1.8,3.0}$			

Note—Same as Table 3 for NGC 2903 ($D = 8.0$ Mpc).

Table 6. NGC 4258 SBF Results

Confirmed			Possible			Background		
Name	SBF S/N	Dist (Mpc)	Name	SBF S/N	Dist (Mpc)	Name	SBF S/N	Dist (Mpc)
NGC 4248	45.0	$7.8^{+0.5,0.9}_{-0.5,1.0}$	dw1218+4623	1.1	$12.7^{+\infty,\infty}_{-4.1,6.2}$	dw1214+4726	0.1	> 12.3
LVJ1218+4655	7.6	$7.6^{+0.7,1.5}_{-0.6,1.1}$	dw1220+4922	4.2	$6.8^{+1.2,2.8}_{-1.0,1.8}$	dw1214+4621	4.6	> 12.0
dw1219+4743	8.6	$7.7^{+0.9,1.8}_{-0.8,1.5}$	dw1220+4748	1.9	$12.7^{+7.4,\infty}_{-3.8,6.3}$	dw1214+4743	-0.5	> 10.7
UGC 7356	22.8	$6.5^{+0.7,1.4}_{-0.7,1.4}$	dw1223+4848	1.2	$10.4^{+12.4,\infty}_{-3.1,4.6}$	dw1216+4709	-0.5	> 10.8
dw1220+4729	5.3	$9.4^{+2.7,6.4}_{-2.0,3.6}$				dw1217+4639	0.4	> 20.2
dw1220+4649	8.7	$7.9^{+1.1,2.3}_{-1.0,1.9}$				dw1217+4703*	1.8	> 4.1
dw1223+4739	19.6	$7.3^{+0.7,1.4}_{-0.7,1.4}$				dw1217+4759	13.3	> 8.5
						dw1217+4747	2.7	> 9.8
						dw1217+4656	9.1	> 10.9
						dw1218+4748	1.6	> 8.2
						dw1218+4801	0.1	> 7.5
						dw1219+4921	1.9	> 8.7
						dw1219+4718	3.8	> 10.3
						dw1219+4727	14.4	> 13.1
						dw1219+4705	1.7	> 13.3
						dw1219+4939	-0.9	> 18.5
						dw1220+4919	3.4	> 7.8
						UGC 7392	17.6	> 12.8
						dw1220+4700	4.9	> 11.9
						UGC7401	13.2	> 12.4
						dw1222+4755	2.4	> 15.8
						dw1223+4920	1.9	> 13.4

Note—Same as Table 3 for NGC 4258 ($D = 7.2$ Mpc).

NGC 4258: NGC 4248 (Sabbi et al. 2018), dw1219p4743 (Cohen et al. 2018), UGC 7356, and LVJ1218+4655 (Karachentsev et al. 2013). The SBF distances agree quite well in these cases. We confirm another three that had no prior distance information. Several of the confirmed background galaxies are worth discussing in detail. The one candidate that is an exception to the criteria outlined at the beginning of this section is **dw1217p4703** which only has a distance lower bound of ~ 4 Mpc. However, Cohen et al. (2018) used *HST* imaging to show that this galaxy is background to NGC 4258. Furthermore, Cohen et al. (2018) showed that dw1219p4705 and dw1220p4700 are also background, which agrees with the SBF results.

Also classified as background are two candidates that Spencer et al. (2014) considered to be confirmed satellites via their redshifts. These two are dw1214+4621 and dw1217+4759. They have fairly strong SBF signals, but it is visually clear that this signal is coming from their irregular morphology. Even with this added power, the SBF results indicated they are background. Neither show any visible SBF which should be quite apparent given their blue colors ($g-r \sim 0.3$). Both of these had redshifts within 250 km/s of NGC 4258. These results do speak a little of the dangers of confirming satellites with only redshifts, especially if there are multiple groups at different distances projected onto the same area of sky, as is the case for NGC 4258. Peculiar velocities can be easily the same magnitude as the velocity dispersion of galaxies in groups of this mass.

Two candidate dwarfs around NGC 4258 have imaging in the *HST* archive: dw1219+4718 and dw1219+4727. In the *HST* images, these galaxies do not resolve into stars, which is expected at $D \sim 7$ Mpc, indicating they are background. This is in line with the SBF results for these two candidates.

5.5. *NGC 4565*

The SBF results for NGC 4565 were fairly inconclusive, as shown in Table 7. Only a few galaxies could be confirmed as either satellites or background. NGC 4562 is fairly irregular so the SBF distance is likely underestimated. Given that the redshift is within 100 km/s of NGC 4565, this galaxy is very likely a companion of NGC 4565. The candidate dw1234p2531 has a SDSS redshift which is quite a bit smaller than NGC 4565 (600 km/s less). This candidate has a very regular, nucleated dSph morphology which means the SBF should be trustworthy. The signal is certainly coming from the SBF of the bulk stellar population. We therefore consider this candidate as a confirmed satellite and note that the SDSS redshift might be inaccurate. Looking at the SDSS spectrum, we believe it is likely that the SDSS pipeline erroneously identified an artifact with Hα emission from the galaxy, leading to a spurious redshift. IC 3571 was too irregular to attempt an SBF measurement but has a redshift consistent with NGC 4565 so we consider it a likely satellite. Zschaechner et al. (2012) noted a bridge in HI between this galaxy and NGC 4565, in line with this conclusion. The candidate dw1235+2606 is located directly in the middle of the HI warp on the northwest edge of the disk of NGC 4565. Radburn-Smith et al. (2014) used HST observations to show that there is a clump of young (~ 600 Myr) stars located in the warp which is likely what our detection algorithm identified as a candidate satellite. They argue that these stars formed in-situ in the warp. In this case, this candidate should not be considered a real satellite, and we include it in the 'background' category. Even though it is associated with the host, it is not a 'satellite'. We note that Gilhuly et al. (2019) interpret this candidate as the core of an accreted satellite whose disruption produced other LSB structures seen in their data.

5.6. *NGC 4631*

Table 8 shows the SBF anaylsis results for NGC 4631. The analysis was quite successful, with 9 confirmed satellites and only one candidate that remains possible/unconfirmed. The unconfirmed satellite, dw1242p3231, is an exception to our usual criteria. It has strong SBF signal that is consistent with being at the distance of NGC 4631. However, it is a small compact system that is projected onto the outskirts of the disk of NGC 4631. Visually, it is unclear whether the signal we measure is coming from this candidate or possibly from outer disk stars of NGC 4631. Since this dwarf is still visible so close to NGC 4631, it is likely that it is on the foreground of (and associated with) NGC 4631. However, we conservatively do not confirm this candidate. The confirmed candidate dw1241p3251 is only barely consistent with the distance of NGC 4631 within 2σ. This galaxy is somewhat non-Sérsic, and so the distance is likely underestimated and likely more consistent with NGC 4631. This galaxy also has a redshift consistent with NGC 4631 ($\Delta cz \sim 60$ km/s). We do not attempt an SBF measurement for NGC 4627, but it is clear this galaxy is physically associated to NGC 4631 both from redshift and ongoing tidal disruption. The SBF distance errorbars for dw1240p3247 are quite large (± 4 Mpc), even though the SBF signal is quite strong. This is driven by the large error on the measured color of this galaxy. This galaxy is the progenitor of a large tidal stream around NGC 4631 and is clearly physically associated. UGCA 292 is a

Table 7. NGC 4565 SBF Results

Confirmed			Possible			Background		
Name	SBF S/N	Dist (Mpc)	Name	SBF S/N	Dist (Mpc)	Name	SBF S/N	Dist (Mpc)
dw1234+2531	9.8	$12.3^{+0.9,1.9}_{-0.9,1.8}$	dw1233+2535	2.0	$9.7^{+3.9,\infty}_{-1.8,2.9}$	dw1238+2536	-0.4	> 13.4
NGC 4562*	11.8	$10.3^{+0.6,1.3}_{-0.6,1.2}$	dw1233+2543	2.6	$13.1^{+3.8,\infty}_{-2.1,3.6}$			
IC 3571	–	–	dw1234+2627	0.8	$13.2^{+\infty,\infty}_{-4.9,7.0}$			
dw1237+2602	9.9	$11.1^{+0.7,1.6}_{-0.7,1.3}$	dw1234+2618	2.0	$7.6^{+3.2,\infty}_{-1.5,2.3}$			
			dw1235+2616	1.0	$15.5^{+\infty,\infty}_{-5.2,7.7}$			
			dw1235+2534	0.4	> 10.4			
			dw1235+2637	0.3	> 4.7			
			dw1235+2609	0.8	$14.4^{+\infty,\infty}_{-5.1,7.5}$			
			dw1235+2606	3.5	$13.5^{+6.1,\infty}_{-4.0,6.6}$			
			dw1236+2616	2.8	$7.0^{+1.9,6.0}_{-1.3,2.2}$			
			dw1236+2603	1.7	$14.9^{+8.9,\infty}_{-3.7,5.9}$			
			dw1236+2634	0.2	> 10.3			
			dw1237+2605	4.4	$8.9^{+1.8,4.2}_{-1.5,2.7}$			
			dw1237+2637	0.8	$13.7^{+\infty,\infty}_{-4.8,6.9}$			
			dw1237+2631	1.6	$7.5^{+4.8,\infty}_{-2.0,3.3}$			
			dw1238+2610	0.9	$9.7^{+\infty,\infty}_{-3.4,5.0}$			

Note—Same as Table 3 for NGC 4565 ($D = 11.9$ Mpc).

Table 8. NGC 4631 SBF Results

Confirmed			Possible			Background		
Name	SBF S/N	Dist (Mpc)	Name	SBF S/N	Dist (Mpc)	Name	SBF S/N	Dist (Mpc)
dw1239+3230	7.6	$7.3^{+0.8,1.6}_{-0.7,1.2}$	dw1242+3231	8.0	$7.1^{+0.6,1.2}_{-0.5,0.9}$	UGCA 292* **give dist**	24.4	> 2.8
dw1239+3251	6.6	$6.1^{+1.6,3.3}_{-1.3,2.4}$				dw1240+3239	9.1	> 10.4
dw1240+3216	10.7	$6.8^{+0.8,1.6}_{-0.7,1.5}$				dw1242+3224	8.8	> 9.9
dw1240+3247	8.8	$7.6^{+6.6,\infty}_{-3.6,5.5}$				dw1242+3227	0.9	> 10.4
dw1241+3251	13.4	$6.3^{+0.5,1.1}_{-0.4,0.8}$				dw1243+3229	17.0	> 8.8
NGC 4627	–	–				dw1243+3232	3.4	> 12.1
dw1242+3237	6.9	$7.2^{+3.0,7.1}_{-2.1,3.7}$						
dw1242+3158	6.1	$7.3^{+1.0,2.2}_{-0.9,1.7}$						
dw1243+3228	19.7	$8.2^{+0.4,0.9}_{-0.4,0.9}$						

Note—Same as Table 3 for NGC 4631 ($D = 7.4$ Mpc). Note that UGCA 292 is not background but significantly in the foreground of NGC 4631.

foreground dwarf galaxy as evidenced by both a TRGB distance (Dalcanton et al. 2009) and the SBF distance. Several of the background galaxies are surprising given their LSB, spheroidal morphology and no clear massive host in the background of NGC 4631. The lack of SBF exhibited by dw1243p3232 (HSC-5) and dw1240p3239 (HSC-7) can be seen in the much deeper HSC imaging of Tanaka et al. (2017). The galaxies are significantly smoother than other (confirmed) candidates of similar color. They would have to be significant outliers to the SBF calibration of Carlsten et al. (2019b) to be at the distance of NGC 4631. We note that the apparent SBF signal coming from the confirmed background galaxy dw1243+3229 is from its irregular morphology and not real SBF. Its redshift is > 250 km/s larger than that of NGC 4631 and is very likely background. dw1242p3227 was too faint to have a robust distance constraint from the CFHT data alone **update table**.

In Appendix C, we confirm these results using the *much* deeper HSC data of Tanaka et al. (2017). The HSC data we use has $\sim$ 15$\times$ more photon collection as the CFHT data (considering telescope aperture and exposure time). The results are remarkably consistent between the two datasets. The HSC data confirms dw1243p3232 (HSC-5) and dw1240p3239 (HSC-7) to be background. The results also show that dw1242p3227 (HSC-1) is background. Thus, we include this dwarf in the background category. The HSC confirms dw1243+3228, dw1241+3251, dw1240+3216, and dw1242+3158 to be at the distance of NGC 4631, with *much* higher S/N. Since dw1242+3231 is still projected on top of the disk of NGC 4631 in the HSC data, this dwarf's status as a satellite is still unclear.

5.7. *NGC 5023*

Due to the shallower data for NGC 5023, we do not confirm any candidates as satellites. As listed in Table 9, one candidate is likely background while the other is unclear from the SBF analysis.

5.8. *M51*

Table 10 gives the SBF results for the candidates found around M51. The one candidate that we confirm, NGC 5229, shows strong SBF and is clearly not far in the background. Sharina et al. (1999) give a brightest-stars distance of 5.1 Mpc which would put it significantly in the foreground of M51. However, they quote a $\pm$2 Mpc uncertainty in that distance. Due to NGC 5229's disky morphology, the SBF results are not very trustworthy. Still, we find an SBF distance of $\sim$ 7.7 Mpc which is likely somewhat underestimated and, therefore, suggestive of association with M51. The redshift of this galaxy is also consistent with being bound to M51 (Δcz $\sim$100 km/s). Thus, we tentatively include this galaxy as a confirmed satellite, but we note that a firm confirmation will likely require an *HST* TRGB distance. There are two candidates, dw1329+4622 and dw1330+4708, that had inconclusive SBF results but had redshifts that indicate they are background. dw1329+4622 has a redshift from Dalcanton et al. (1997). dw1330+4708 has a photometric redshift from SDSS that indicates it's far in the background. However, we suspect this redshift might be quite erroneous, and we include this candidate in the 'possible' category.

5.9. *M64*

Carlsten et al. (2019c) only found one candidate satellite in the vicinity of M64, at least partly due to the small survey footprint and shallow data. As shown in Table 11, the SBF analysis indicates that this dwarf is background.

5.10. *M104*

The SBF results for M104, shown in Table 12, are quite promising. Due to the good seeing of the data and brightness of SBF in the i band, we were able to confirm a large number of the candidates to be at the distance of M104 (D = 9.55 Mpc). A few of the dwarfs were exceptions to our usual classification criteria. dw1240m1140 showed a strong SBF signal that put it significantly in the foreground. However, this dwarf is located very close to M104 in projection, and the halo of M104 could be adding signal to the SBF measurement causing the distance to be underestimated. Considering its dSph morphology, proximity to M104, and SBF, we suspect this dwarf is physically associated with M104. The SBF measurement of dw1242m1116 indicated that it is background, but this dwarf only partially fell on a chip in the MegaCam data which might make the measurement unreliable. Thus, we include this dwarf in the unconfirmed/possible category. dw1238m1122 was contaminated by a large saturation spike in the MegaCam data and so we did not attempt an SBF measure of this galaxy.

5.11. *Summary*

As demonstrated in the previous sections, the SBF results were overall quite promising. For some of the hosts (e.g. NGC 4258, NGC 4631, NGC 1023) a majority of the candidates could be either confirmed as satellites or as background contaminants. For almost all hosts, some candidates were unconstrained by the SBF analysis. In most cases, these candidates were very LSB and/or small and the S/N was not high enough to set meaningful constraints with the SBF. In some cases, the candidates were very irregular or had other problems (e.g. saturation spike or chip gap) that prevented an SBF measurement. Other hosts had very uncertain SBF results. NGC 4565, in particular, had mostly unconstrained candidates. This is mostly due to the larger distance to this host (12 Mpc) and the fact that the data used was r band and not i band which has brighter SBF.

Overall **xx** of the **xx** candidates of Carlsten et al. (2019c) are confirmed as physical satellites while **xx** are constrained to be background. While SBF appears to be a powerful and efficient distance indicator for LSB dwarfs, it is possible that a few of the candidates of our sample are misclassified. Carlsten et al. (2019b) did not find any large ($> 2\sigma$) outliers to their SBF calibration so it is unlikely the SBF distances could be wrong due

Table 9. NGC 5023 SBF Results

Confirmed			Possible			Background		
Name	SBF S/N	Dist (Mpc)	Name	SBF S/N	Dist (Mpc)	Name	SBF S/N	Dist (Mpc)
			dw1314+4420	0.2	$21.2^{+\infty,\infty}_{-12.7,15.4}$	dw1310+4358	-0.8	> 11.0

Note—Same as Table 3 for NGC 5023 ($D = 6.5$ Mpc).

Table 10. M51 SBF Results

Confirmed			Possible			Background		
Name	SBF S/N	Dist (Mpc)	Name	SBF S/N	Dist (Mpc)	Name	SBF S/N	Dist (Mpc)
NGC 5195	30.0	$7.7^{+0.3,0.6}_{-0.3,0.6}$	dw1327+4637	-0.9	> 5.8	dw1327+4654	3.5	> 8.7
NGC 5229*	30.0	$7.7^{+0.3,0.6}_{-0.3,0.6}$	dw1327+4626	1.3	$10.5^{+12.5,\infty}_{-3.0,4.6}$	dw1328+4718	6.7	> 12.3
			dw1328+4703	2.3	$6.7^{+2.4,11.6}_{-1.3,2.2}$	dw1329+4634	0.8	> 13.7
			dw1330+4731	1.6	$12.5^{+8.8,\infty}_{-3.6,5.8}$	dw1329+4622*	2.9	> 6.9
			dw1331+4654	-0.1	> 5.4	dw1330+4708*	1.6	> 7.1
			dw1331+4648	0.6	$14.8^{+\infty,\infty}_{-5.7,7.8}$	dw1330+4720	2.2	> 15.2
						dw1332+4703	0.4	> 10.2
						dw1333+4725	2.6	> 13.3

Note—Same as Table 3 for M51 ($D = 8.6$ Mpc).

Table 11. M64 SBF Results

Confirmed			Possible			Background		
Name	SBF S/N	Dist (Mpc)	Name	SBF S/N	Dist (Mpc)	Name	SBF S/N	Dist (Mpc)
						dw1255+2130	3.3	> 5.8

Note—Same as Table 3 for M64 ($D = 5.3$ Mpc).

to unusual stellar populations. Instead, the risk is point sources (e.g. star clusters and/or H II regions) or irregular morphologies adding spurious fluctuation power into the measurement, causing a background galaxy to appear closer than it is. We carefully visually checked all of the fits and masks used in the SBF to ensure that any SBF signal is coming from the bulk stellar population. However, it is possible that some candidates, especially the small ones which would only have a few bright clumps of SBF are mis-measured. The other major risk in this measurement is if the color of the candidate is very incorrect. Due to the LSB nature of these galaxies, it is possible that the measured color is significantly wrong. We estimate the error in the galaxy colors using image simulations which should, in principle, capture the systematic uncertainty associated with the sky subtraction. However, it is possible that significant systematic errors linger that are not represented in the estimated uncertainty in the color. If the galaxy was measured to be bluer than it actually is, the SBF distance can be greatly overestimated and vice versa. The most likely failure mode in this regard is a galaxy being measured bluer than it actually is and being (erroneously) constrained to the background because it does not exhibit the strong SBF expected for blue galaxies.

6. CLEANED SAMPLE OF SATELLITES

In this section, we give some overview of the sample of satellites confirmed using SBF and the other information presented in the previous section. We provide analogous

Table 12. M104 SBF Results

Confirmed			Possible			Background		
Name	SBF S/N	Dist (Mpc)	Name	SBF S/N	Dist (Mpc)	Name	SBF S/N	Dist (Mpc)
dw1237-1125	5.5	$7.5^{+2.1,4.7}_{-1.8,3.3}$	dw1238-1208	0.5	$14.6^{+\infty,\infty}_{-7.9,10.7}$	dw1237-1110	2.2	> 11.3
dw1239-1152	5.3	$8.5^{+1.3,2.9}_{-1.1,2.0}$	dw1238-1116	3.8	$9.3^{+2.6,6.5}_{-1.9,3.4}$	dw1240-1155	7.8	> 20.5
dw1239-1159	6.2	$11.3^{+1.5,3.2}_{-1.2,2.3}$	dw1238-1122	–	–	dw1241-1210	3.2	> 12.7
dw1239-1143	21.9	$9.4^{+0.6,1.2}_{-0.6,1.3}$	dw1238-1102	2.4	$9.1^{+3.6,14.8}_{-2.0,3.4}$			
dw1239-1113	13.7	$7.9^{+1.2,2.4}_{-1.1,2.3}$	dw1239-1154	3.1	$7.2^{+2.2,5.9}_{-1.6,2.8}$			
dw1239-1120	12.5	$9.8^{+0.6,1.2}_{-0.6,1.1}$	dw1239-1118	1.9	$10.9^{+5.0,\infty}_{-2.3,3.9}$			
dw1239-1144	7.9	$9.1^{+1.5,3.3}_{-1.3,2.5}$	dw1239-1106	0.2	> 8.7			
dw1240-1118	33.7	$8.6^{+0.6,1.2}_{-0.6,1.3}$	dw1241-1123	0.2	$24.4^{+\infty,\infty}_{-14.2,17.1}$			
dw1240-1140*	5.6	$4.2^{+0.6,1.3}_{-0.5,1.1}$	dw1241-1105	2.7	$8.3^{+2.3,7.8}_{-1.5,2.7}$			
dw1241-1131	5.1	$7.1^{+1.2,2.7}_{-1.1,2.0}$	dw1242-1116*	1.7	$14.8^{+8.5,\infty}_{-3.3,5.1}$			
dw1241-1153	6.5	$10.9^{+1.2,2.7}_{-1.1,2.2}$	dw1242-1129	1.5	$13.7^{+10.9,\infty}_{-3.6,5.7}$			
dw1241-1155	16.2	$9.0^{+0.7,1.5}_{-0.8,1.6}$	dw1243-1137	2.2	$5.6^{+2.0,10.7}_{-1.2,2.0}$			

Note—Same as Table 3 for M104 ($D = 9.55$ Mpc).

figures to those in Carlsten et al. (2019c) showing the color and structural parameters of the confirmed satellites. Tables giving the properties of the confirmed and possible satellites, including physical sizes and absolute luminosities are given in Appendix A. For the physical quantities, we assume the confirmed and possible satellites are at the distance of the host, instead of using the individual SBF distances.

6.1. *Colors of Satellites*

The vast majority of the MW satellites are quenched, spheroidal systems. The only two that are not are the LMC and SMC. It is interesting to ask if this is common for other MW-like systems. The SAGA Survey (Geha et al. 2017) has found that the vast majority (26 out of 27) of satellites that they have confirmed via spectroscopy around 8 nearby MW-analogs are actually star-forming. They are sensitive to $M_r < -12.3$ which would include five MW satellites (LMC, SMC, Sgr, Fornax, and Leo I). Carlsten et al. (2019c) found that the colors of the candidate satellites were generally red, presumably similar to the MW satellites, and somewhat redder than the SAGA satellites. It is quite possible that this is due to the larger spread in host mass in the sample of Carlsten et al. (2019c), which includes some hosts significantly more massive than the MW (e.g. M104) that are contributing a lot of red satellites. The more massive hosts presumably have more efficient quenching mechanisms (e.g. ram pressure stripping via a hot halo). Splitting the sample by host stellar mass would be interesting, but we likely do not have the necessary statistics with the current sample of confirmed satellites. Combining the current sample with the other known nearby hosts (MW, M31, CenA, M81, M101, M94) might yield enough satellites to compare different host stellar masses, but that is out of the scope of the current paper. Instead, in this paper, we will simply consider the color distribution of the confirmed

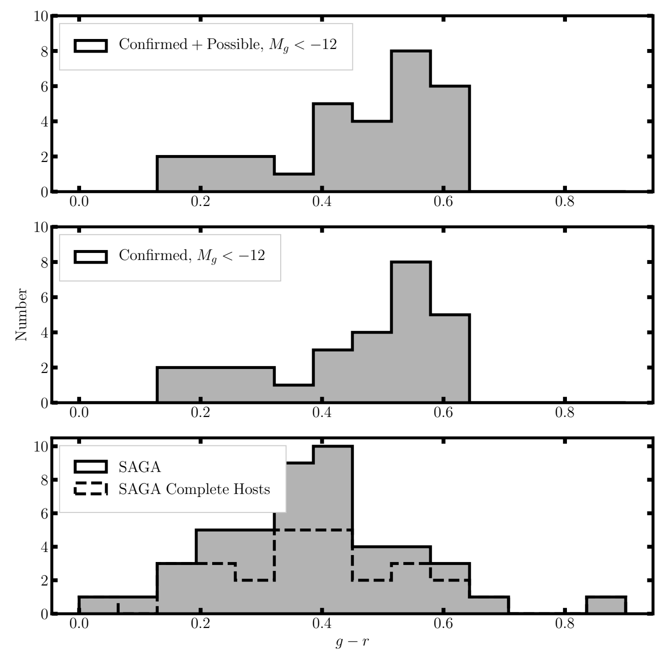

Figure 3. The $g-r$ colors of the confirmed satellites and the possible satellites. Both samples are restricted to $M_g < -12$. Bottom plot shows the colors of the SAGA satellites.

and possible satellites and see if they are different from the entire population of candidates of Carlsten et al. (2019c).

Figure 3 shows the color distribution of the confirmed satellites along with the distribution of the confirmed and possible satellites. Since almost all of the candidates that remained in the possible/unconfirmed category were very faint, the two distribution are about the same since we only include galaxies brighter than $M_g = -12$. The colors of the confirmed satellites appear to be fairly similar to those of the overall sample of Carlsten et al. (2019c) and somewhat redder than the SAGA satellites. We will explore how much of this can be explained by the wider range in stellar masses of our hosts in future work.

6.2. *Structural Parameters*

Figure 4 shows various structural parameters for the confirmed satellites of the 10 hosts. They show close agreement with the scaling relations of the MW and M31 classical satellites. The confirmed satellite shows better agreement with the LG dwarfs than the entire sample shown in Carlsten et al. (2019c). Many of the objects in Carlsten et al. (2019c) were smaller than the LG dwarfs at fixed luminosity, indicating they were likely background. As seen in all three panels of Figure 4, the surface brightness completeness of Carlsten et al. (2019c) is $\mu_{0,V} \sim 26$ mag arcsec^{-2}

7. SATELLITE LUMINOSITY FUNCTIONS IN THE LOCAL VOLUME

In this section, we first collect together from the literature the properties of satellites around the nearby hosts that have been previously surveyed. As discussed in the Introduction, there are six nearby systems ($D < 7$ Mpc) that have been well searched for satellites. All of the satellites in these systems have been confirmed with distance measurements and the surveys are complete down to at least $M_V \sim -10$ over a large fraction of the virial volume. We give an overview of the literature that gives the satellites properties in the next section, along with estimates of the completeness for each system. We end this section with the luminosity functions of all known nearby systems, including the new satellite systems from the current work.

7.1. *Previously Surveyed Systems*

For reproducibility, we list all of the satellite properties for each host in tables in Appendix A. Positions and luminosities for the MW classical satellites are taken from McConnachie (2012). The distances are taken from the compilation of Fritz et al. (2018) and individual references are given in the Appendix. We alter the luminosities from McConnachie (2012) to account for the different distances. We assume that the census of MW classical satellites is complete throughout the virial volume. For the luminosity function, we assume the MW has a stellar mass of 5×10^{10} $M_\odot$Bland-Hawthorn & Gerhard (2016) and mass to light ratio of $M/L_V \sim 2$.

We take the sample of M31 satellites from Martin et al. (2016) and McConnachie et al. (2018). The distances come from a variety of sources, prioritizing *HST* distances over ground-based and variable star over TRGB, where possible. References are given in the Appendix. We assume a stellar mass of M31 of 10.3×10^{10} $M_\odot$ Sick et al. (2015) and $M/L_V \sim 2$ to calculate M_V. The PandAS survey is sensitive to ultra-faint satellites of M31 with $M_V \lesssim -6$ but only covers the inner projected 150 kpc volume. However, with Pan-STARRS the census of M31 satellites is likely complete through the virial volume down to $M_V \sim -9$ (e.g. Martin et al. 2013a,b). The luminosities come from McConnachie et al. (2018), altered to account for the updated distances.

The satellites of Centaurus A come from Crnojević et al. (2019) and Müller et al. (2019). Crnojević et al. (2019) estimate their completeness at 90% for dwarfs brighter than $M_V \sim -9$ over their Magellan/Megacam survey footprint which roughly covers the inner projected 150 kpc. Similarly, Müller et al. (2019) estimate that they are complete down to $M_V \sim -10$ over the inner projected 200 kpc.

The list of satellites of M81 comes from Chiboucas et al. (2013) and Chiboucas et al. (2009). The photometry for NGC 3077, M81, M82, NGC 2976, IC 2574, and DDO 82 come from Gil de Paz et al. (2007). The photometry for IKN, BK5N, KDG061, and KDG064 come from the recent HSC imaging of Okamoto et al. (2019). The rest come from Chiboucas et al. (2013). We convert the r magnitudes reported in Chiboucas et al. (2013) into V magnitudes assuming $M_V \sim M_r + 0.4$ (Crnojević et al. 2019). The TRGB distances come from Chiboucas et al. (2013) and Karachentsev et al. (2013). We do not include any of the dwarfs that Chiboucas et al. (2013) consider to be tidal dwarf galaxies. We assume that the census of satellites of M81 is complete for all 'classical'-like satellites ($M_V \lesssim -8$) throughout the inner projected 250 kpc volume **update figures with this new bound**.

The satellite system of M101 comes from Tikhonov et al. (2015), Danieli et al. (2017), Carlsten et al. (2019a), and Bennet et al. (2019). The photometry for M101 uses the updated distance of Beaton et al. (2019). To convert from the B magnitudes reported by Tikhonov et al. (2015), we assume $M_V \sim M_B - 0.3$.

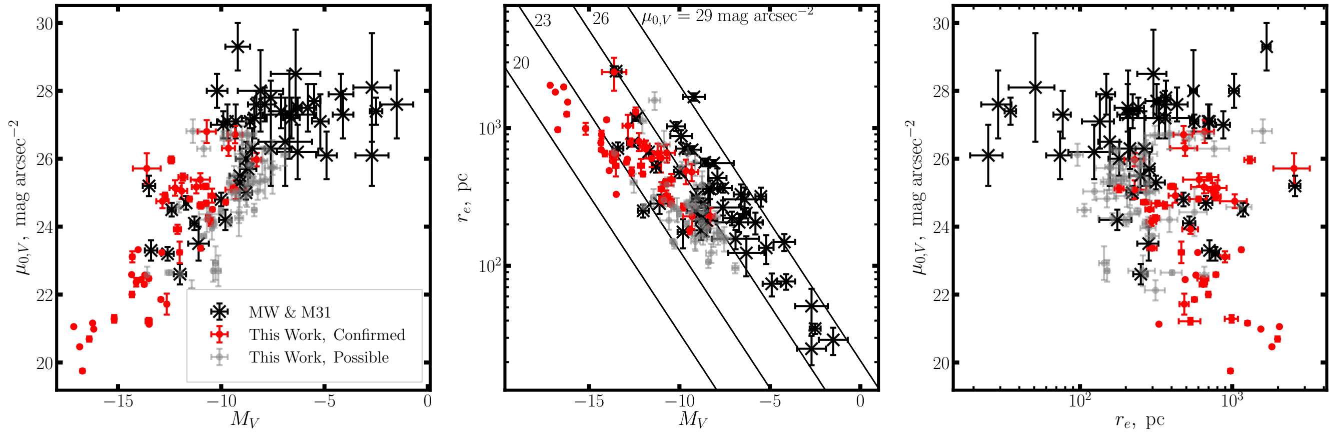

Figure 4. Structural parameters of the confirmed satellites (red). Shown in black are the MW and M31 satellites from McConnachie (2012). The gray points show the possible/unconfirmed satellites from the current work. Generally these are smaller and have lower surface brightness than the confirmed satellites.

We use the *HST* photometry of Bennet et al. (2019) for dwA and dw9. We use the *HST* photometry for DF1, DF2, and DF3 (S. Danieli, priv. comm.). We note that the magnitudes we take for these objects are significantly ($\sim 1-2$ mag) brighter than those listed by Bennet et al. (2019). Carlsten et al. (2019a) suggests that UGC 8882 could feasibly be a satellite but that the SBF distance puts it $\sim$ 2 Mpc behind M101[1]. Their SBF distance agrees quite well with that of Rekola et al. (2005) who use a completely different calibration so we assume it is a field dwarf in the background of M101. We assume that the satellite system of M101 is complete down to $M_V \sim -8$ within the inner projected 200 kpc (see Fig 1 of Carlsten et al. 2019a).

The properties of the satellites of M94 come from Smercina et al. (2018). We assume the census is complete to $M_V \sim -9$ throughput the inner projected 150 kpc volume.

7.2. *Luminosity Functions*

In this section, we compare the luminosity functions of the previously known systems with the systems that we have characterized in this work. As discussed in §5, the SBF analysis was more successful for some hosts than others. In this section and when comparing with models below, we only consider the systems where the SBF was able to confirm a large fraction of the candidates as either real satellites or background and which also had significant survey coverage. As shown in Carlsten et al. (2019c), 6 of the ten LV hosts had coverage over most of the inner projected 150 kpc. These six are NGC 1023, NGC 4258, NGC 4565, NGC 4631, M51, and M104. Due to their smaller survey footprint and ambiguous SBF results, we do not further consider the other four hosts. For every one of the six hosts that we do consider, there were still some candidates that were neither confirmed as satellites or as background galaxies. We kept them in the 'unconfirmed/possible' satellites category. This uncertainty will mean there is a spread in the LF and we give both the upper and lower bounds on what the LF can be. Considering the dynamic range in luminosity that the LFs cover, we do not consider the photometric errors of the satellite luminosities in constructing the LFs. Several of the satellites in the tables of Appendix A are marked by ** to indicate that their photometry is suspect. These galaxies were markedly non-Sérsic, and the photometry comes from fitting Sérsic profiles to these galaxies. In these cases, we estimate the systematic errors to still be significantly less than a magnitude and, thus, relatively insignificant in constructing the LFs.

Instead of considering all of these systems together, we split the hosts into two groups based on mass. Much of the host-to-host scatter will be due to different host masses and not due to the physics of stochastic dwarf galaxy formation. Since halo mass is not easily measured, we only attempt to roughly split the sample into two groups. In splitting the hosts, we take into account the stellar mass, the peak circular velocity, and any dynamical estimate of the halo mass from the kinematics of satellites.

The nearby hosts seem to naturally split into 'MW-sized' hosts and hosts that are slightly more massive, which we term 'small group'. The MW-sized halos are

[1] With the uncertainty quoted by Carlsten et al. (2019a), UGC 8882 was $\sim 2\sigma$ behind M101. However they assumed a large (0.1 mag) uncertainty in the color measurement. Estimating the uncertainty in the color with the more realistic image simulation approach taken in Carlsten et al. (2019c), we get an SBF distance of 8.5 ± 0.6 Mpc which is $> 3\sigma$ behind M101.

those with halo mass roughly in the range $0.8-3\times10^{12}$ $M_\odot$, and the small groups have halo mass in the range $3-8\times10^{12}$. The MW is clearly in the first group (e.g. Callingham et al. 2019; Watkins et al. 2019). Based on their stellar mass and peak rotation speed, we put NGC 4565, NGC 4631, and M51 into this group as well[2] (see Carlsten et al. (2019c) for these quantities). Karachentsev & Kudrya (2014) use the kinematics of groups members and their projected separation to estimate the dynamical masses of several of our hosts from a virial theorem-like mass estimator. They estimate a dynamical mass of $3\pm1\times10^{12}$ $M_\odot$ for NGC 4258. Considering that some of the group members included might not be actual group members (many do not have redshift-independent distances), this is an upper limit to the halo mass. Thus, we include NGC 4258 in the MW-like group. Similarly, Karachentsev & Kudrya (2014) estimate a dynamical mass for M94 of $2.7\pm0.9\times10^{12}$ $M_\odot$. This mass might even be more overestimated since the nearest group member they consider is at a projected separation of >250 kpc. Considering its stellar mass and rotation speed as well, we include M94 in the MW-like group. Tikhonov et al. (2015) estimate the dynamical mass of M101 as 0.75×10^{12} $M_\odot$. Karachentsev & Kudrya (2014) estimate it slightly higher at $1.5\pm1\times10^{12}$ $M_\odot$. Both estimates put it in the MW-like group. Finally, a variety of estimates for the virial mass of M31 put it around $\sim1.5\times10^{12}$ $M_\odot$(e.g. Watkins et al. 2010; González et al. 2014; Peñarrubia et al. 2014). Even though its stellar mass is $\sim2\times$ that of the MW, we include it in the MW-like group.

The remaining four hosts (M81, CenA, NGC 1023, and M104) constitute the 'small-group' category. Karachentsev & Kudrya (2014) estimate the dynamical mass of the M81 group as $5\pm1\times10^{12}$ $M_\odot$which is significantly above that of the MW. Similarly, those authors estimate the dynamical mass of CenA to be $7\pm2\times10^{12}$ $M_\odot$, consistent with the estimate of Woodley (2006). Karachentsev & Kudrya (2014) estimate the mass of the M104 halo to be $30\pm20\times10^{12}$ $M_\odot$. While this is ostensibly above the upper end of our 'small-group' mass range, this estimate might be quite overestimated due to the inclusion of objects without redshift independent distances. Additionally, most of the group members considered are separated by $\gg200$ kpc projected from M104, increasing the uncertainty in this estimate. We include M104 in the small-group category but note that it might be even more massive. Trentham & Tully (2009) estimate a dynamical mass of the NGC 1023 group to be $\sim6\times10^{12}$ $M_\odot$which fits right into the small-group category.

As we will see below, this distinction by halo mass of the hosts is also reflected in the LFs. The small-group hosts have significantly richer satellite systems than the MW-analogs. We note that the small-group hosts are different from the MW-analogs in other ways as well. The small-group hosts include the only two ellipticals in the whole sample (M104 and CenA).

Figure 5 shows the cumulative luminosity functions for the hosts considered here, split roughly by halo mass. To deal with the very different survey coverage for the different hosts, only satellites within 150 kpc (3D distance for the MW and M31, projected for the other hosts) are included, but further area correction is not done. The completeness limits of the previously surveyed hosts were given in the previous section. For the hosts surveyed in the current work, the completeness limit is estimated in Carlsten et al. (2019c) and is generally $M_V\sim-9$ over the survey footprint.

We note a few interesting things in Figure 5. First, there is quite a bit of scatter between hosts. Presumably some of this is due to the different coverage for the different hosts. This will be accounted for more realistically when comparing with models below. The scatter would be even more if we compared the two mass bins together, emphasizing the importance of considering them separately. There are some very large magnitude gaps present, particularly M94, CenA, and M104 show large gaps between the largest and second largest member in each group. Interestingly, CenA and M104 are the only two ellipticals in the whole sample, and their merging history might be reflected in these magnitude gaps. To interpret these luminosity functions further, we need to compare with predictions from theoretical models, which is what we turn to next.

8. THEORETICAL MODELS

We compare the observed satellite systems with those predicted from dark matter only (DMO) simulations combined with abundance matching (AM). The two alternatives to this are to use the results from hydrodynamic simulations (obviating the need to use AM) or to use a semi-analytic model (SAM) combined with a DMO simulation. We do not use a hydrodynamic simulation because the public hydrodynamic simulations (e.g. Illustris and EAGLE) do not have the baryonic resolution to comfortably resolve satellites of the luminosity

[2] The stellar masses of NGC 4565 and M51 (7.6×10^{10} $M_\odot$ and 6×10^{10} $M_\odot$, respectively) might indicate that they occupy more massive host halos. However, their satellite systems are clearly far less rich than the hosts we include in the 'small-group' category, like M81 and NGC 1023, and we consider these hosts to more likely be MW-analogs.

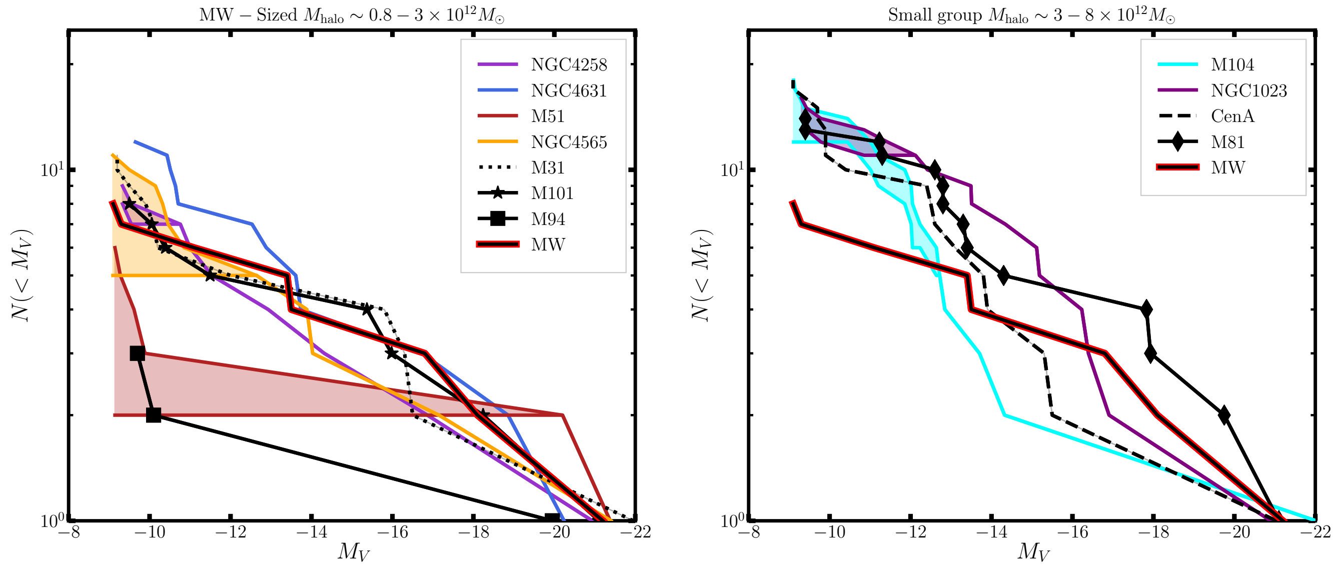

Figure 5. The cumulative luminosity functions for the 12 LV hosts that have been well surveyed for satellites. The hosts are split roughly by halo mass, see text for details. The MW is shown in the right panel for comparison. The spread in some of the LFs indicates the uncertainty in group membership for the candidates where the SBF analysis was ambiguous. All hosts are restricted to the inner 150 kpc radius but further area corrections are not done. The luminosity completeness is different for each host but is $M_V \lesssim -9$ in all cases.

that we are concerned with. Even the non-public hydrodynamic zoom simulations (e.g. FIRE and APOSTLE) would not be ideal because the simulation suites just include a small number of hosts (10 in the case of FIRE (e.g. Garrison-Kimmel et al. 2019)) which is not suitable to explore the host-to-host scatter. While SAMs could be used to explore the properties of satellites of virtually any mass, their added complication over AM makes extracting simple physical interpretations somewhat difficult. Therefore, we use halo catalogs from DMO simulations combined with a stellar-halo mass relation (SHMR) to populate the halos as the basis for the theoretical models used here.

8.1. *DMO Simulation*

For the DMO simulations, we use the halo catalogs from the Illustris-TNG100 project (Nelson et al. 2019; Pillepich et al. 2018; Springel et al. 2018; Nelson et al. 2018; Naiman et al. 2018; Marinacci et al. 2018) and the high-resolution ELVIS zoom simulations (Garrison-Kimmel et al. 2014). Each simulation has its strength. TNG has a better constraint on the host-to-host scatter because of the number of MW-like hosts (> 1000) in the simulated volume which is much more than the 48 simulated hosts in the ELVIS project. On the other hand, the higher resolution of ELVIS allows us to consider the effect of very large scatter in the SHMR. While TNG resolves the subhalos that likely host the classical satellites, it will be incomplete for subhalos of any lower mass. Large scatter in the SHMR means that very low mass subhalos might host fairly bright satellites and, thus, subhalos significantly below the mass of the classical satellites need to be resolved.

While the baryonic results of TNG will not resolve the satellites we are interested in (baryonic particle mass $\sim 10^6$ M$_\odot$), the DM particle mass of 7.5×10^6 M$_\odot$ means that subhalos hosting the satellites we are focusing on ($M_{\rm vir} \sim 5 \times 10^9$ M$_\odot$, see below) will be fairly resolved. Note that we do not use the explicit DMO TNG simulation. Instead, we use the dark matter halo catalog of the full baryonic run. This will capture any affect that the baryons might have on the halo abundances. In particular, this should capture the enhanced destruction of subhalos by the baryonic disk which has been shown to have a dramatic impact on subhalo abundance, particularly near the host galaxy (e.g. D'Onghia et al. 2010; Garrison-Kimmel et al. 2017b; Kelley et al. 2019).

We select host halos from the friends-of-friends group catalog provided in the TNG public data release. For comparison with the MW-sized hosts, we select halos with M_{200} in the range $0.8 - 3 \times 10^{12}$ M$_\odot$. For comparison with the small-group hosts, we select halos in the range $3 - 8 \times 10^{12}$ M$_\odot$. To avoid any problems with the periodic boundary conditions, we only select halos that are more than 1.5 Mpc from a simulation box edge. Additionally, we only select FoF halos whose most massive subhalo (which will be occupied by the host galaxy) is at least 0.6×10^{12} M$_\odot$ for the MW-like halos and 2.25×10^{12} M$_\odot$ for the small-group halos. This is a minor restriction, and will result in systems comparable to our hosts where there is clearly a dominant galaxy surrounded by lower mass companions. After these cuts, we end up with xx MW-like hosts and xx of the more massive hosts. We then use the SubFind catalog of subhalos to procure a list of subhalos in each FoF group. The most massive of these is the host galaxy, and the rest are the satellites.

The ELVIS suite consists of 24 isolated MW sized hosts and 12 pairs of hosts in a LG-like configuration. We treat all 48 of these hosts in the same way. The ELVIS hosts range in mass fairly uniformly between 1 and $3{\times}10^{12}$ $\mathrm{M}_\odot$. While this does cover the range we expect for the MW-sized observed hosts, due to the halo mass function (e.g. Tinker et al. 2008), it is more likely that an observed host occupies a $10^{12}\mathrm{M}_\odot$ halo than a $3\times10^{12}\mathrm{M}_\odot$ halo. Therefore, we expect that the ELVIS hosts to be, in general, more rich in subhalos than the corresponding MW-like hosts from TNG.

8.2. *Stellar-Halo Mass Relation*

With a catalog of subhalos in hand, we populate the halos with luminous galaxies using a SHMR. We use the peak virial mass of each subhalo, M_{peak}, to determine the stellar mass of the galaxy. This is important to account for the effect of tidal stripping once a halo becomes a subhalo of a more massive galaxy. To determine M_{peak}, we use the TNG merger trees and record the peak virial mass that each subhalo attains along its main progenitor branch. The ELVIS halo catalogs list M_{peak}.

The well-known SHMRs from abundance matching (e.g. Behroozi et al. 2013; Moster et al. 2013) are only defined for $M_* \gtrsim 10^7$ $\mathrm{M}_\odot$ which is larger than the stellar masses of many satellites in our sample. It is possible to extrapolate these relations down, but it is known that the SHMR of Behroozi et al. (2013) will over-predict the luminosity function of MW and M31 satellites (Garrison-Kimmel et al. 2014). A steeper relation between stellar mass and halo mass is needed. The steeper Moster et al. (2013) relation is actually too steep and will under-predict the LF of the LG Garrison-Kimmel et al. (2017a).

We take as our fiducial SHMR the relation from Garrison-Kimmel et al. (2014) and Garrison-Kimmel et al. (2017a). This relation has the same functional form as the Behroozi et al. (2013) SHMR but uses a steeper power law slope at the low mass end. Garrison-Kimmel et al. (2014) used the GAMA stellar mass function (Baldry et al. 2012) to infer a power law slope of -1.92 ($M_* \propto M_{\mathrm{halo}}^{-1.92}$), as opposed to the slope of -1.412 inferred in Behroozi et al. (2013) using an SDSS-derived stellar mass function. Garrison-Kimmel et al. (2014) showed that this SHMR could reproduce the stellar mass function of LG dwarfs down to $M_* \sim 5\times10^5$ $\mathrm{M}_\odot$. Garrison-Kimmel et al. (2017a) found that a slightly shallower slope of -1.8 fits the LG dwarf stellar mass functions a little better. Thus, as our fiducial model, we use the functional form of the Behroozi et al. (2013) SHMR but modified to have a power law slope of -1.8 at the low mass end ($M_{\mathrm{halo}} \lesssim 10^{11.5}$ $\mathrm{M}_\odot$). All of the parameters other than the low mass slope are taken from Behroozi et al. (2013). For the fiducial model, we assume a fixed lognormal scatter of 0.2 dex about this relation. While, the scatter in the SHMR will likely increase for lower halo masses (e.g. Munshi et al. 2017), there is no current understanding of what functional form it should take or how large it should be. Thus we assume the scatter is the same as it is constrained to be at higher masses (e.g. Behroozi et al. 2013).

This SHMR is well reproduced in several high-resolution zoom hydrodynamic simulations. Both the FIRE (Fitts et al. 2017) and NIHAO (Buck et al. 2019) projects produce galaxies that fall on or near this relation (see Figure 6 of Garrison-Kimmel et al. (2017a) for a detailed comparison with simulation results). In particular, Buck et al. (2019) find a SHMR with a slope of -1.89 for their simulated dwarf satellites, very similar to the slope we adopt here. We note, however, that there is still significant scatter in the predicted SHMR among different simulation projects (see e.g. Agertz et al. 2020). The SHMR inferred by Read et al. (2017) is significantly shallower than the one we use here (see also the simulation results of Read et al. 2016). It is possible that this relation is shallower because it is inferred from field dwarfs, not satellites. Satellites experience both tidal stripping and quenching by their massive host which will make the SHMR less steep and steeper, respectively, depending on which process is dominant (Read & Erkal 2019). However, the results of Buck et al. (2019) show no difference in the SHMR between field and satellite dwarfs. We leave a detailed comparison of the different SHMRs found in the literature to future work.

The SHMR is used to assign a stellar mass to each subhalo. We assume a fixed mass-to-light ratio of $M_*/L_V = 1.2$ to convert this stellar mass into a V band magnitude. This mass-to-light ratio is roughly the average ratio inferred for the MW satellites (Woo et al. 2008).

One additional consideration to note about the AM model is that we do not account for the possibility of dark subhalos. Presumably, some very low mass subhalos exist that do not contain a luminous galaxy as the UV background associated with cosmic reionization completely suppressed star formation in those halos.

The mass scale at which this process becomes important is often estimated as a few $\times 10^9$ $M_\odot$ (e.g. Okamoto et al. 2008; Okamoto & Frenk 2009; Sawala et al. 2016b; Ocvirk et al. 2016), however recent work is pushing this scale down to smaller masses (e.g. Wheeler et al. 2019; Graus et al. 2019). These masses are at the low end of (or well below) the halo masses expected for classical-sized satellites so we do not expect this to be a relevant physical process for the type of satellites we consider here.

9. RESULTS

In this section, we show the results of comparing the observed satellite systems to the ones predicted from the AM model described above. We show three main comparisons. First, we compare the observed luminosity functions for each observed host to those predicted from the models. We separately consider the 'MW-like' hosts and the 'small-group' hosts. Second, we explore the number of satellites as a function of host stellar mass. This allows us to consider the 'MW-like' hosts and the 'small-group' hosts simultaneously. This comparison demonstrates that the scatter between observed satellite systems closely matches that predicted by our model, once the mass of the host is accounted for. Finally, we look more closely at the average shape of the LFs by comparing the combined LF of all observed systems to the simulated systems to show that, while the number of satellites agrees between observations and simulations, the observed hosts have more bright satellites and fewer faint systems than the models predict.

9.1. *Individual Luminosity Functions*

We compare the observed LFs with those predicted from the models in Figure 6 for the 8 'MW-sized' hosts. Each thin black line represents one of the IllustrisTNG hosts and the spread in the models is shown by the blue shaded regions. To account for the very different survey area coverage between the observed hosts, for each observed host, the models are forward modeled through the survey area selection function for that specific host. For the previously surveyed systems, the area coverage for each host is given in §7.1. For comparison with the MW and M31, all model satellites within 300 kpc of the host are included. For the hosts surveyed in the current work, the area coverage of each host is taken from the survey footprints shown in Figure 1 of Carlsten et al. (2019c). For each observed host (other than the MW and M31), the model hosts are mock observed from a random direction at the distance of the real host and satellite galaxies are selected that project into the survey footprint. For the non-circular footprints shown in Figure 1 of Carlsten et al. (2019c), a random direction is taken to be North.

To account for uncertainties in the distances to the dwarf satellites, model satellites are selected that fall within **500** kpc of the host along the line of sight. This will include some splash-back satellites and field dwarfs that haven't yet fallen into their host, but presumably the observed satellite systems include a few of these dwarfs as well. The 500 kpc limit is chosen as a compromise between the hosts that have had their satellites confirmed with TRGB[3] and those that have had their satellites confirmed with SBF[4]. The forward modelling of the simulated satellite systems explains why the models predict different number of satellites for the different hosts in Figure 6.

For the systems which had inconclusive SBF distance constraints for some of their candidate satellites, Figure 6 shows the spread of possible LFs, given the uncertain/possible members.

There are several interesting things to note from Figure 6. First is that the normalization of the LF of the MW is very well reproduced by the AM model. This confirms the result of Garrison-Kimmel et al. (2017a) that this SHMR can reproduce the stellar mass function of MW satellites quite well. Second is that while there is large spread between the observed systems, the luminosity functions all fall within the $\pm 2\sigma$ spread of the models. While M94 is clearly a deficient satellite system, it is still slightly within the $\pm 2\sigma$ spread of the models. We explore the scatter between systems in more detail in the next section.

In Appendix B, we show the comparison between the observed LFs and those predicted using the ELVIS high-resolution zoom DMO simulations. The results are fairly similar to Figure 6, demonstrating that the resolution of IllustrisTNG does not appear to be affecting our results. The ELVIS predicted LFs are noticeably richer than the TNG LFs because the ELVIS host halos are more massive, on average, than the TNG 'MW-like' hosts, as discussed above. A secondary reason is that the ELVIS subhalos do not experience the enhanced tidal disruption of the central disk, like the TNG subhalos do.

Figure 7 shows the analogous results for the more massive ('small-group') hosts. The increased richness of these satellite systems is well reproduced in the AM model. There are fewer hosts of this mass in the TNG-100 volume, and this is reflected in the fewer number of

[3] *HST* TRGB can yield distances accurate to 5% which at $D =$ 7 Mpc is ~ 300 kpc.

[4] SBF, as applied here, can yield distances accurate to 15% which at $D = 7$ Mpc is ~ 1 Mpc.

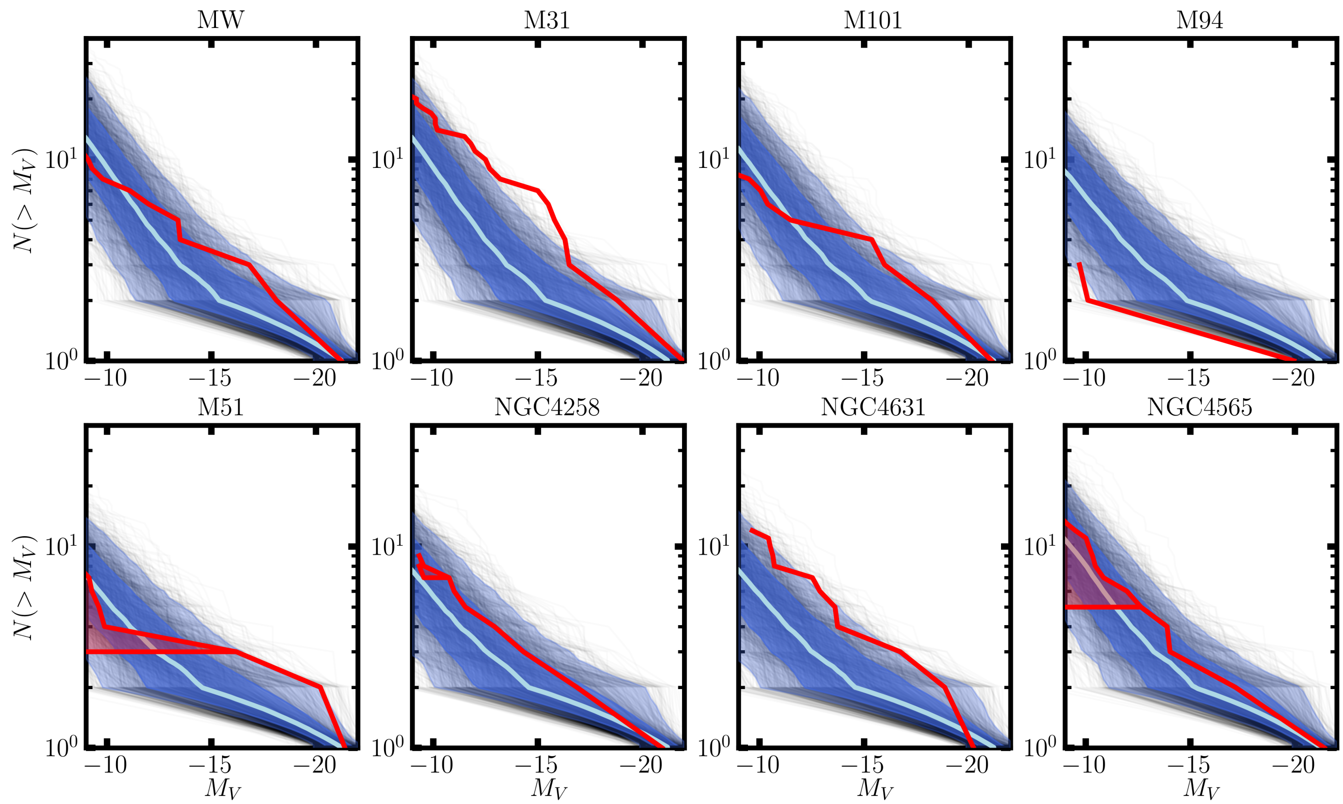

Figure 6. The cumulative luminosity functions for the 8 'MW-sized' hosts that have been well surveyed for satellites (red). The thin black lines show the predicted LFs from the abundance matching model described in the text. The blue regions show the $\pm 1, 2\sigma$ spread in the models. The luminosity completeness is different for each host but is $M_V \sim -9$ in all cases. For each host, the model satellite systems have been forward modeled considering the survey area selection function for that specific host. For the hosts that had inconclusive results from the SBF distances, a spread of possible LFs is shown, accounting for uncertain membership.

model lines in Figure 7. While still within the scatter of the models, M104 and CenA show a larger than typical magnitude gap between first and second brightest group member. It is feasible that this is related to the elliptical morphology of these two galaxies, but we leave further exploration of this to future work.

9.2. *Satellite Richness versus Stellar Mass*

More massive halos are expected to host more subhalos of a certain mass. While we have rough halo mass estimates for each host in our sample (see above) these estimates are not accurate enough to explore how satellite richness depends on halo mass. Instead, in this section we explore how satellite richness depends on stellar mass, which we use as a proxy for halo mass. More massive (in stellar mass) hosts should host more satellites above a certain luminosity limit. The scatter in this relation should partly come from scatter in the SHMR for the hosts and partly from host-to-host variance in the amount of substructure. The main goal of this section is to quantify the host-to-host scatter in the observations and compare with that of the models.

Figure 8 shows the relation between satellite richness and stellar mass for both the observed hosts and the simulated hosts. Both the 'MW-sized' and 'small-group' hosts are plotted together. To account for the different area coverage of the different hosts, only the satellites within 150 projected kpc are included, and we assume each observed host is complete to this radius. This is certainly a little optimistic and could be contributing some scatter. For the MW and M31, for which we have detailed 3D locations of the satellites, the observed satellite systems are mock "re"-observed at a distance of 7 Mpc. The errorbars show the spread ($\pm 1\sigma$) in the satellite number for many different viewing directions. For the systems with inconclusive SBF results, the errorbars show the spread ($\pm 1\sigma$) in possible satellite richness ac-

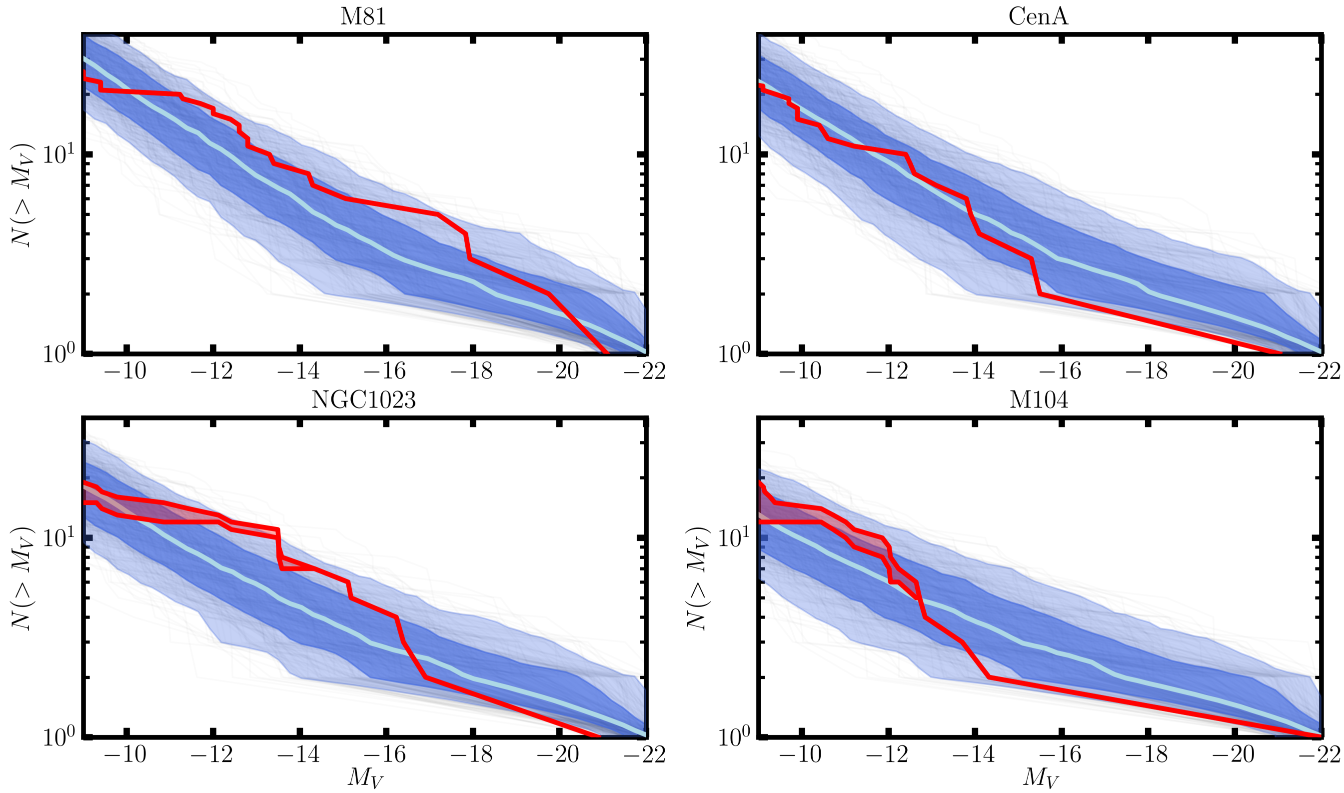

Figure 7. The cumulative luminosity functions for the 4 'small-group' hosts that have been well surveyed for satellites (red). The thin black lines show the predicted LFs from the abundance matching model described in the text. The blue regions show the $\pm 1, 2\sigma$ spread in the models. The luminosity completeness is different for each host but is $M_V \sim -9$ in all cases. For each host, the model satellite systems have been forward modeled considering the survey area selection function for that specific host. For the hosts that had inconclusive results from the SBF distances, a spread of possible LFs is shown, accounting for uncertain membership.

counting for this uncertainty[5]. The simulated systems are mock observed at a distance of 7 Mpc. Only satellites brighter than $M_V < -9$ are included. The observed hosts should all be fairly complete to this magnitude, however differing completeness levels at this magnitude might contribute some of the scatter as well. For the simulations, the stellar mass used for each host is the actual stellar mass for that host predicted by the hydrodynamic component of IllustrisTNG, not a stellar mass from abundance matching.

There is clearly a positive relation between host stellar mass and satellite richness, in both the observed hosts and the simulated hosts. The observed hosts appear to bracket the region populated by the simulated hosts fairly well. The purple line shows the average trend of the simulated hosts. While the observations all fall in the spread of the models, they seem to exhibit a steeper relation between satellite number and host stellar mass than the model predictions. It is unclear if this is a result of the particular SHMR we use. More observed systems are likely needed to conclusively show that this relation agrees or not between the observations and models. We note that a slightly shallower SHMR would somewhat steepen the predicted satellite richness versus host stellar mass relation. We leave a full exploration of this to future work.

The right panel of Figure 8 shows the number of satellites corrected for the general trend of the models with host stellar mass. Both the models and observations are fairly symmetric around zero, indicating that the SHMR we use accurately reproduces the normalization of the satellite luminosity functions. Also shown in the plot is the rms scatter of the observed systems and the simulated systems. They agree fairly well, indicating that the host-to-host scatter in the observed systems is what one would expect from the models, once variations in the host mass are accounted for. The scatter in the observed hosts is actually somewhat below the scatter in the simulated hosts. Interestingly, framed this way it

[5] Specifically, each uncertain member is given a 50-50 chance of being a real satellite.

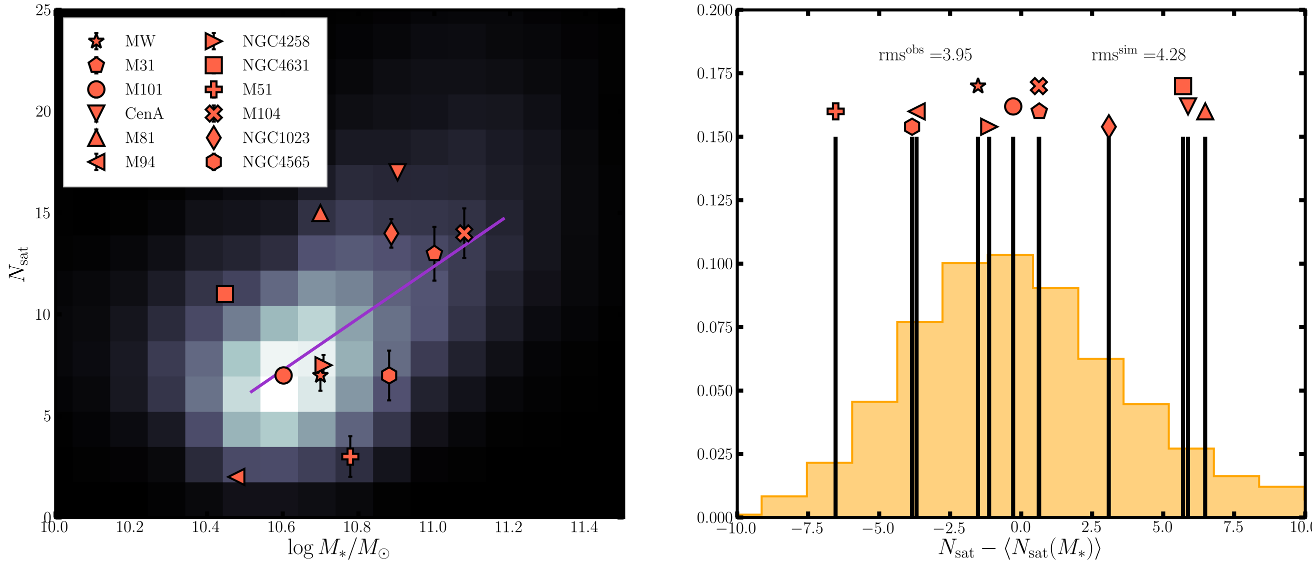

Figure 8. Left: the number of satellites $M_V < -9$ within a projected radius of 150 kpc for each observed host (indicated by the symbols) as a function of host stellar mass. The background color-map shows the results for the simulated hosts. The simulated hosts are hosts drawn from Illustris-TNG100 combined with the stellar halo mass relation (SHMR) of Garrison-Kimmel et al. (2017a). The purple line shows the average relation for the simulated hosts. Right: the residual in the number of satellites, corrected for the average relation of the simulated hosts. The rms scatter agrees fairly well between the simulated and observed hosts.

appears M51 is even more deficient in satellites than the M94 system, considering its higher stellar mass.

This result shows that the observed host-to-host scatter in satellite richness amongst nearby MW-like systems agrees with that predicted by ΛCDM simulations without the need of greatly increased scatter in the SHMR. Thus, we do not confirm the results of Smercina et al. (2018) who argued that significantly increased scatter is required to explain M94's satellite system. We come to a different conclusion for two reasons. First, we show that much of the observed scatter between hosts is due to the difference in host halo masses (as proxied by stellar mass) and this is important to correct for when inferring host-to-host scatter. Second, we consider 12 observed systems which offers much improved statistics over the 5 considered by Smercina et al. (2018). With this said, it certainly is possible that a SHMR with large scatter could also reproduce the host-to-host scatter, but we've at least shown that it is not needed. We will explore actually fitting for a SHMR to determine the best fitting slope and scatter in future work.

9.3. *Average LF Shape*

In the last section, we showed that the number of satellites agrees well between observations and simulations. In this section, we explore the shape of the LFs in more detail. To do this, we construct the average differential luminosity function of the 12 observed hosts and compare with the average differential luminosity functions of the simulated hosts. Figure 9 shows this comparison for satellites with $M_V < -9$ and within a projected separation of 150 kpc of their host. We assume all 12 observed hosts are complete at this level. To account for the effect of projection angle on the satellite systems of the MW and M31, many different projection angles are averaged over. Uncertain membership of some satellites are also accounted for by averaging over all possible realizations of the uncertain satellites being members or not.

We use the ELVIS suite to be able to explore the effects of very high scatter in the SHMR. Subhalos around the simulated hosts are selected in the same way as in the previous section. We take 50 random viewing angles for each of the 48 ELVIS hosts. To account for the fact that we are comparing with all observed systems (including the 'small-group' hosts), we renormalize the ELVIS hosts, using the fact that subhalo abundance is independent of host halo mass if subhalo mass is normalized by the host mass (e.g. Springel et al. 2008). We renormalize 2/3 of the ELVIS hosts to have a host mass of 1.5×10^{12}M$_\odot$ and the remaining 1/3 to have a host mass of 5×10^{12}M$_\odot$[6]. We compare the observed aver-

[6] We find qualitatively the same result if we do not do this renormalization. The normalization of the average LF is slightly lower without it as the ELVIS halos are MW-like and, therefore, likely lower mass than our 'small-group' hosts, but the shape discrepancy is even more pronounced in this case.

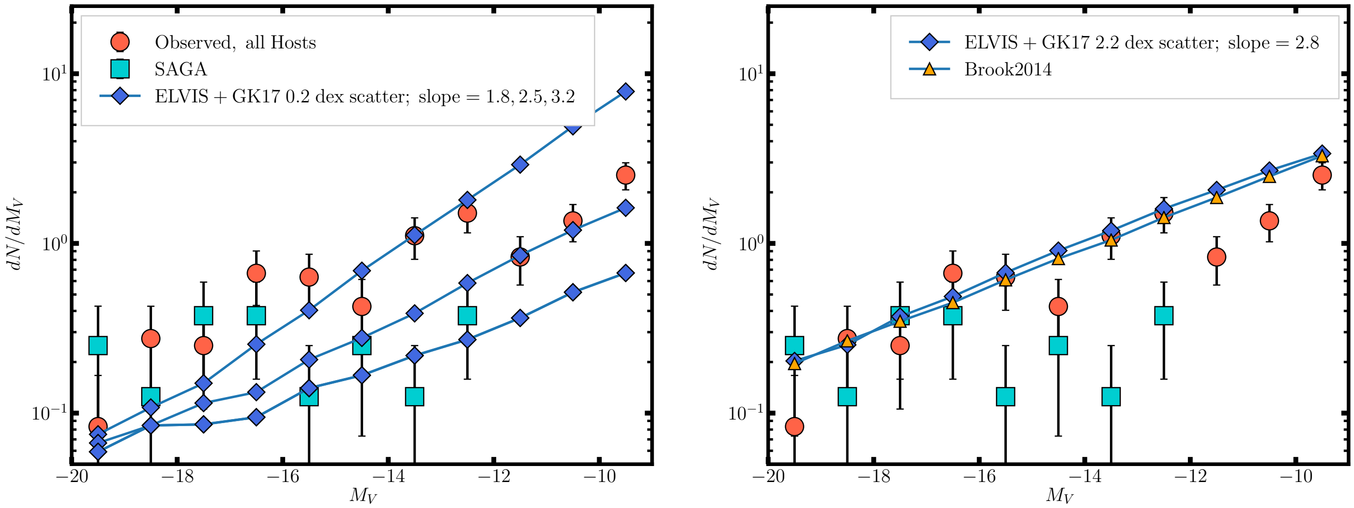

Figure 9. *Left*: The average differential LF of all 12 observed hosts we consider. The average SAGA (Geha et al. 2017) LF is shown in turquoise. The SAGA results agree well with the Local Volume hosts for the bright satellites ($M_V < -14$), but include fewer faint satellites. The average simulated LF is shown in blue. The simulated LF uses the ELVIS zoom in simulations combined with a stellar halo mass relation (SHMR). Curves corresponding to three different values of the low mass slope of the SHMR of Garrison-Kimmel et al. (2017a) are shown. The smallest slope value corresponds to the highest (most rich) LF. Note that no matter the slope used in the SHMR, the simulated LF cannot match the shape of the observed LF. There are too many observed bright satellites. *Right*: The same observational samples are shown compared to the average simulated LF using the SHMR of Garrison-Kimmel et al. (2017a) but now assuming a large ~ 2 dex scatter. Also shown is the simulated LF using the SHMR of Brook et al. (2014) which has a higher normalization than Garrison-Kimmel et al. (2017a) and produces more bright satellites.

age LF to the average simulated LF using the fiducial SHMR (with low mass slope of 1.8) along with the result of using a slope of 2.5 and 3.2. This figure shows that no matter the low mass slope used in the SHMR of Garrison-Kimmel et al. (2017a), the average simulated LF will not quite match the shape of the observed LF. The observed LF has too many bright satellites and an overall flatter LF. We show on the right side of Figure 9 that the shape of the observed LF can be matched if we use a SHMR with very large ($\sim$2 dex) scatter or use a SHMR with higher normalization like that of Brook et al. (2014). Both of these changes increase the number of bright satellites in the simulated hosts, bringing them into agreement with the observations.

We also compare the average observed LF of the 8 MW analogs of the first SAGA release (Geha et al. 2017). In comparing with the SAGA results, we assume $M_V \sim M_r + 0.2$. These galaxies also show a surplus of bright satellites and a flatter LF slope. This was noticed by Geha et al. (2017) and Zhang et al. (2019). The SAGA hosts appear to have fewer satellites in the range $-14 < M_V < -12$ than our observed hosts, possibly indicating some incompleteness in the SDSS catalogs used in SAGA. We estimate that 8 out of our 12 hosts would qualify as 'MW-analogs' according to the criteria of Geha et al. (2017) so this is a fairly reasonable comparison. Only one (M104) is above the accepted range of M_K ($-23 < M_K < -24.6$), and one (NGC 4631) is actually below this range. Two others (M51 and M81) would not qualify due to the presence of bright nearby companion (NGC 5195 and M82, respectively).

It appears that the observed systems are the most discrepant from the simulated hosts around $M_V \sim -16$ to -17 but they are in surplus at brighter, LMC-like magnitudes as well. Several observational results have argued that Magellanic Cloud (MC) analogs are fairly rare around MW-analogs (e.g. Tollerud et al. 2011; Liu et al. 2011). Liu et al. (2011) argue that 80% of MW-analogs in SDSS do not have any MC-like satellite within a projected 150 kpc, with 11% having one and 4% having two. They define a MC-analog as a satellite between 2 and 4 magnitudes fainter than the host. We note that 6 (NGC 1023[7], NGC 4631, MW, M31[8], M81, and M101) of the 12 LV hosts would qualify as having one or more MC-analogs according to this definition. Similarly 6 out of 8 of the SAGA hosts have at least one satellite within 2 and 4 magnitudes fainter than the host and within 150 kpc projected. Liu et al. (2011) define a MW-analog as having $-21.4 < M_r < -21.0$. Most of the SAGA

[7] Using the R band magnitudes of NGC 1023 and IC 239 in Trentham & Tully (2009), IC 239 would not qualify, but using the V band magnitudes we use here, it (barely) does.

[8] Depending on whether M33 is projected within 150 kpc.

hosts are within this range while some of our hosts are above and some are below. We leave a more detailed exploration of this possible tension to future work.

10. CONCLUSIONS

In this paper, we have taken the catalogs of candidate satellites around 10 massive hosts in the LV from Carlsten et al. (2019c) and measured the distances to the candidate satellites to confirm membership. We used the same CFHT imaging used in Carlsten et al. (2019c) to measure the SBF of the candidate satellites and constrain their distance from that. Since many of the hosts used r band imaging instead of i which does not have a modern SBF calibration, we first derive an SBF calibration for the r band based on $g-r$ color. This calibration is based on the TRGB-anchored calibration of Carlsten et al. (2019b) and uses SSP models to convert into r. The inferred calibration agrees quite well with the relatively few galaxies we could find that have r band imaging and literature TRGB distances.

The SBF results were overall quite promising. With the SBF analysis, there are three possible outcomes for each candidate satellite. If the SBF signal was strong (S/N$\gtrsim$**5**) and the distance consistent with the distance to the host, we confirmed the candidate as a physical satellite of the host. If the 2σ lower bound to the SBF distance was beyond the distance to the host, we confirmed the candidate as background. In these cases, the dwarf would have measurable SBF if it were at the distance of the host. Its lack of SBF constrains it to be in the background. Finally, for the smallest and faintest candidates, the SBF measurements were too low S/N to make any firm statements about the distance. In this category, we also conservatively include a handful of galaxies that we did not attempt an SBF measurement on because they were too irregular or had some other issue that would interfere with the SBF.

For one host (NGC 4631) that has existing extremely deep HSC imaging data, we confirm the SBF results that we found with the CFHT data. This gives confidence in the distances and distance lower bounds that we derive using the relatively shallow CFHT data for the other hosts. These distance constraints are not just a result of the S/N of the imaging data as we get the same results using significantly deeper data.

In total we confirm **xx** candidates as real satellites via SBF, including **xx** that were previously confirmed via TRGB. A further **xx** are confirmed via other distance measures available in the literature, particularly TRGB and redshift. The SBF results constrain **xx** candidates to be background, and redshift measurements from the literature constrain a further **xx** to be background. The remaining **xx** candidates are still unconstrained. Deeper imaging or (most likely) *HST* will be required to ascertain the distances to these candidates.

Since the unconstrained galaxies are generally the faintest and/or smallest candidates, the satellite systems of the hosts we surveyed are generally clean of contaminants down to $M_g\sim-9$ to -10 and complete to that magnitude within the area coverage of the search footprint. There were six hosts (NGC 1023, NGC 4258, NGC 4565, NGC 4631, M51, and M104) that had fairly promising SBF results and whose survey footprint was a significant portion of the host's virial volume. The remaining four (NGC 1156, NGC 2903, NGC 5023, and M64) either had ambiguous SBF results with most candidates remaining unconstrained or had very limited survey area coverage. For the first group of well-surveyed systems, we explore the luminosity functions of these satellite systems in more detail. We combine this sample of six with a sample of six nearby hosts that have been previously well-surveyed by previous work. This is by far the largest sample of nearby roughly MW-sized hosts whose satellite systems have surveyed for satellites down to approximately the faintest classical satellites. Instead of considering all of these systems together, we separately consider the hosts that are the most MW-like (NGC 4258, NGC 4565, NGC 4631, M51, MW, M31, and M101) and the hosts that are somewhat more massive (NGC 1023, M104, CenA, M81), which we refer to as 'small-group' hosts.

To interpret the luminosity functions of the observed satellite systems, we develop a simple model based on DMO cosmological simulations coupled with a SHMR inferred from abundance matching. Luminous galaxies are painted onto the DMO results with a SHMR. The fiducial SHMR we use is known to reproduce the normalization of the luminosity function of the MW and agrees fairly well with the results of high resolution hydrodynamic zoom simulations from multiple groups. The predicted satellite systems from this model are able to well reproduce both the normalization and spread of the observed satellite systems, for both the 'MW-like' hosts and the 'small-group' hosts.

We consider the satellite richness as a function of the host stellar mass, which we use as a rough proxy for the host halo mass. Both the observed systems and simulated systems show a clear positive relation between satellite number and host stellar mass. Using this relation, we quantitatively show that the observed systems exhibit the same host-to-host scatter as the simulated systems once host mass is accounted for, without the need to invoke increased scatter in the SHMR.

Finally, we consider the average shape of the observed differential LF and compare the average simulated LF. We find that while the simulations combined with a reasonable SHMR can produce the right total number of satellites, the simulations under-produce bright satellites and over-produce faint ones. We note that increasing the scatter in the SHMR (to ~ 2 dex) or increasing the normalization of the SHMR (e.g Brook et al. 2014) can bring the LF shapes into better agreement. We find that our average LF agrees quite well with the initial SAGA results which show a similar surplus of bright satellites. The LV systems do show more fainter ($M_V \sim -13$) satellites than the SAGA results, however.

While our sample of satellite systems would benefit from further distance measurements (particularly *HST* TRGB distances), it is currently fairly cleaned and can be used to explore other aspects of small-scale structure formation. We provide tables of the measured properties of the confirmed (and possible) satellites in the Appendix. In a companion paper, we explore the radial distribution of satellites in this sample and compare with ΛCDM simulations.

ACKNOWLEDGEMENTS

Support for this work was provided by NASA through Hubble Fellowship grant #51386.01 awarded to R.L.B.by the Space Telescope Science Institute, which is operated by the Association of Universities for Research in Astronomy, Inc., for NASA, under contract NAS 5-26555. J.P.G. is supported by an NSF Astronomy and Astrophysics Postdoctoral Fellowship under award AST-1801921. J.E.G. is partially supported by the National Science Foundation grant AST-1713828. S.G.C acknowledges support by the National Science Foundation Graduate Research Fellowship Program under Grant No. #DGE-1656466.

Based on observations obtained with MegaPrime/MegaCam, a joint project of CFHT and CEA/IRFU, at the Canada-France-Hawaii Telescope (CFHT) which is operated by the National Research Council (NRC) of Canada, the Institut National des Science de l'Univers of the Centre National de la Recherche Scientifique (CNRS) of France, and the University of Hawaii.

Software: `SExtractor` (Bertin & Arnouts 1996), `sep` (Barbary 2016), `Scamp` (Bertin 2006), `SWarp` (Bertin 2010), `astropy` (Astropy Collaboration et al. 2018), `imfit` (Erwin 2015)

REFERENCES

Agertz, O., Pontzen, A., Read, J. I., et al. 2020, MNRAS, 491, 1656

Astropy Collaboration, Price-Whelan, A. M., Sipőcz, B. M., et al. 2018, AJ, 156, 123

Baldry, I. K., Driver, S. P., Loveday, J., et al. 2012, MNRAS, 421, 621

Barbary, K. 2016, JOSS, 1, 58

Beaton, R. L., Seibert, M., Hatt, D., et al. 2019, ApJ, 885, 141

Behroozi, P. S., Wechsler, R. H., & Conroy, C. 2013, ApJ, 770, 57

Bellazzini, M., Ferraro, F. R., Origlia, L., et al. 2002, AJ, 124, 3222

Bellazzini, M., Gennari, N., & Ferraro, F. R. 2005, MNRAS, 360, 185

Bennet, P., Sand, D. J., Crnojević, D., et al. 2019, arXiv e-prints, arXiv:1906.03230

—. 2017, ApJ, 850, 109

Bertin, E. 2006, in Astronomical Society of the Pacific Conference Series, Vol. 351, Astronomical Data Analysis Software and Systems XV, ed. C. Gabriel, C. Arviset, D. Ponz, & S. Enrique, 112

Bertin, E. 2010, SWarp: Resampling and Co-adding FITS Images Together, Astrophysics Source Code Library, , , ascl:1010.068

Bertin, E., & Arnouts, S. 1996, A&AS, 117, 393

Blakeslee, J. P., Jordán, A., Mei, S., et al. 2009, ApJ, 694, 556

Bland-Hawthorn, J., & Gerhard, O. 2016, ARA&A, 54, 529

Bonanos, A. Z., Stanek, K. Z., Szentgyorgyi, A. H., Sasselov, D. D., & Bakos, G. Á. 2004, AJ, 127, 861

Bosch, J., Armstrong, R., Bickerton, S., et al. 2018, PASJ, 70, S5

Boulade, O., Charlot, X., Abbon, P., et al. 2003, in Proc. SPIE, Vol. 4841, Instrument Design and Performance for Optical/Infrared Ground-based Telescopes, ed. M. Iye & A. F. M. Moorwood, 72–81

Boylan-Kolchin, M., Bullock, J. S., & Kaplinghat, M. 2011, MNRAS, 415, L40

—. 2012, MNRAS, 422, 1203

Bressan, A., Marigo, P., Girardi, L., et al. 2012, MNRAS, 427, 127

Brook, C. B., Di Cintio, A., Knebe, A., et al. 2014, ApJL, 784, L14

Buck, T., Macciò, A. V., Dutton, A. A., Obreja, A., & Frings, J. 2019, MNRAS, 483, 1314

Byun, W., Sheen, Y.-K., Park, H. S., et al. 2020, arXiv e-prints, arXiv:2001.08342

Callingham, T. M., Cautun, M., Deason, A. J., et al. 2019, MNRAS, 484, 5453

Cantiello, M., Blakeslee, J. P., Ferrarese, L., et al. 2018, ApJ, 856, 126

Carlsten, S. G., Beaton, R. L., Greco, J. P., & Greene, J. E. 2019a, ApJL, 878, L16

—. 2019b, ApJ, 879, 13

Carlsten, S. G., Greco, J. P., Beaton, R. L., & Greene, J. E. 2019c, arXiv e-prints, arXiv:1909.07389

Carlsten, S. G., Strauss, M. A., Lupton, R. H., Meyers, J. E., & Miyazaki, S. 2018, MNRAS, 479, 1491

Carrera, R., Aparicio, A., Martínez-Delgado, D., & Alonso-García, J. 2002, AJ, 123, 3199

Cautun, M., Bose, S., Frenk, C. S., et al. 2015, MNRAS, 452, 3838

Chiboucas, K., Jacobs, B. A., Tully, R. B., & Karachentsev, I. D. 2013, AJ, 146, 126

Chiboucas, K., Karachentsev, I. D., & Tully, R. B. 2009, AJ, 137, 3009

Choi, J., Dotter, A., Conroy, C., et al. 2016, ApJ, 823, 102

Cohen, Y., van Dokkum, P., Danieli, S., et al. 2018, ApJ, 868, 96

Conn, A. R., Ibata, R. A., Lewis, G. F., et al. 2012, ApJ, 758, 11

Coppola, G., Marconi, M., Stetson, P. B., et al. 2015, ApJ, 814, 71

Crnojević, D., Sand, D. J., Caldwell, N., et al. 2014, ApJ, 795, L35

Crnojević, D., Sand, D. J., Bennet, P., et al. 2019, ApJ, 872, 80

Dalcanton, J. J., Spergel, D. N., Gunn, J. E., Schmidt, M., & Schneider, D. P. 1997, AJ, 114, 635

Dalcanton, J. J., Williams, B. F., Seth, A. C., et al. 2009, ApJS, 183, 67

Danieli, S., van Dokkum, P., Merritt, A., et al. 2017, ApJ, 837, 136

D'Onghia, E., Springel, V., Hernquist, L., & Keres, D. 2010, ApJ, 709, 1138

Erwin, P. 2015, ApJ, 799, 226

Fiorentino, G., Contreras Ramos, R., Tolstoy, E., Clementini, G., & Saha, A. 2012, A&A, 539, A138

Fitts, A., Boylan-Kolchin, M., Elbert, O. D., et al. 2017, MNRAS, 471, 3547

Fritz, T. K., Battaglia, G., Pawlowski, M. S., et al. 2018, A&A, 619, A103

Fukugita, M., Shimasaku, K., & Ichikawa, T. 1995, PASP, 107, 945

Garrison-Kimmel, S., Boylan-Kolchin, M., Bullock, J. S., & Lee, K. 2014, MNRAS, 438, 2578

Garrison-Kimmel, S., Bullock, J. S., Boylan-Kolchin, M., & Bardwell, E. 2017a, MNRAS, 464, 3108

Garrison-Kimmel, S., Wetzel, A., Bullock, J. S., et al. 2017b, MNRAS, 471, 1709

Garrison-Kimmel, S., Hopkins, P. F., Wetzel, A., et al. 2019, MNRAS, 487, 1380

Geha, M., Wechsler, R. H., Mao, Y.-Y., et al. 2017, ApJ, 847, 4

Gil de Paz, A., Boissier, S., Madore, B. F., et al. 2007, ApJS, 173, 185

Gilhuly, C., Hendel, D., Merritt, A., et al. 2019, arXiv e-prints, arXiv:1910.05358

González, R. E., Kravtsov, A. V., & Gnedin, N. Y. 2014, ApJ, 793, 91

Graus, A. S., Bullock, J. S., Kelley, T., et al. 2019, MNRAS, 488, 4585

Greco, J. P., Greene, J. E., Strauss, M. A., et al. 2018, ApJ, 857, 104

Gullieuszik, M., Held, E. V., Rizzi, L., et al. 2008, MNRAS, 388, 1185

Hamanowicz, A., Pietrukowicz, P., Udalski, A., et al. 2016, AcA, 66, 197

Ibata, R. A., Lewis, G. F., Conn, A. R., et al. 2013, Nature, 493, 62

Irwin, J. A., Hoffman, G. L., Spekkens, K., et al. 2009, ApJ, 692, 1447

Jensen, J. B., Tonry, J. L., Barris, B. J., et al. 2003, ApJ, 583, 712

Jerjen, H. 2003, A&A, 398, 63

Jerjen, H., Binggeli, B., & Barazza, F. D. 2004, AJ, 127, 771

Jerjen, H., Freeman, K. C., & Binggeli, B. 1998, AJ, 116, 2873

—. 2000, AJ, 119, 166

Jerjen, H., Rekola, R., Takalo, L., Coleman, M., & Valtonen, M. 2001, A&A, 380, 90

Karachentsev, I. D., & Kudrya, Y. N. 2014, AJ, 148, 50

Karachentsev, I. D., Makarov, D. I., & Kaisina, E. I. 2013, AJ, 145, 101

Karachentsev, I. D., Riepe, P., Zilch, T., et al. 2015, Astrophysical Bulletin, 70, 379

Kelley, T., Bullock, J. S., Garrison-Kimmel, S., et al. 2019, MNRAS, 487, 4409

Kim, E., Kim, M., Hwang, N., et al. 2011, MNRAS, 412, 1881

Kinemuchi, K., Harris, H. C., Smith, H. A., et al. 2008, AJ, 136, 1921

Klypin, A., Kravtsov, A. V., Valenzuela, O., & Prada, F. 1999, ApJ, 522, 82

Kuehn, C., Kinemuchi, K., Ripepi, V., et al. 2008, ApJL, 674, L81
Liu, L., Gerke, B. F., Wechsler, R. H., Behroozi, P. S., & Busha, M. T. 2011, ApJ, 733, 62
Marigo, P., Girardi, L., Bressan, A., et al. 2017, ApJ, 835, 77
Marinacci, F., Vogelsberger, M., Pakmor, R., et al. 2018, MNRAS, 480, 5113
Martin, N. F., Schlafly, E. F., Slater, C. T., et al. 2013a, ApJL, 779, L10
Martin, N. F., Slater, C. T., Schlafly, E. F., et al. 2013b, ApJ, 772, 15
Martin, N. F., Ibata, R. A., Lewis, G. F., et al. 2016, ApJ, 833, 167
Martínez-Vázquez, C. E., Stetson, P. B., Monelli, M., et al. 2016, MNRAS, 462, 4349
Martínez-Vázquez, C. E., Monelli, M., Bernard, E. J., et al. 2017, ApJ, 850, 137
Mateo, M., Fischer, P., & Krzeminski, W. 1995, AJ, 110, 2166
McConnachie, A. W. 2012, AJ, 144, 4
McConnachie, A. W., Irwin, M. J., Ferguson, A. M. N., et al. 2005, MNRAS, 356, 979
McConnachie, A. W., Irwin, M. J., Ibata, R. A., et al. 2009, Nature, 461, 66
McConnachie, A. W., Ibata, R., Martin, N., et al. 2018, ApJ, 868, 55
Mieske, S., Hilker, M., & Infante, L. 2006, A&A, 458, 1013
Mieske, S., Hilker, M., Infante, L., & Mendes de Oliveira, C. 2007, A&A, 463, 503
Monachesi, A., Trager, S. C., Lauer, T. R., et al. 2011, ApJ, 727, 55
Moore, B., Ghigna, S., Governato, F., et al. 1999, ApJ, 524, L19
Moster, B. P., Naab, T., & White, S. D. M. 2013, MNRAS, 428, 3121
Müller, O., Jerjen, H., & Binggeli, B. 2015, A&A, 583, A79
—. 2017, A&A, 597, A7
—. 2018a, A&A, 615, A105
Müller, O., Pawlowski, M. S., Jerjen, H., & Lelli, F. 2018b, Science, 359, 534
Müller, O., Rejkuba, M., Pawlowski, M. S., et al. 2019, arXiv e-prints, arXiv:1907.02012
Munshi, F., Brooks, A. M., Applebaum, E., et al. 2017, arXiv e-prints, arXiv:1705.06286
Naiman, J. P., Pillepich, A., Springel, V., et al. 2018, MNRAS, 477, 1206
Nelson, D., Pillepich, A., Springel, V., et al. 2018, MNRAS, 475, 624
Nelson, D., Springel, V., Pillepich, A., et al. 2019, Computational Astrophysics and Cosmology, 6, 2
Ocvirk, P., Gillet, N., Shapiro, P. R., et al. 2016, MNRAS, 463, 1462
Okamoto, S., Arimoto, N., Ferguson, A. M. N., et al. 2019, ApJ, 884, 128
Okamoto, T., & Frenk, C. S. 2009, MNRAS, 399, L174
Okamoto, T., Gao, L., & Theuns, T. 2008, MNRAS, 390, 920
Park, H. S., Moon, D.-S., Zaritsky, D., et al. 2019, ApJ, 885, 88
—. 2017, ApJ, 848, 19
Pawlowski, M. S. 2018, Modern Physics Letters A, 33, 1830004
Pawlowski, M. S., & Kroupa, P. 2013, MNRAS, 435, 2116
—. 2019, MNRAS, 2774
Pawlowski, M. S., Pflamm-Altenburg, J., & Kroupa, P. 2012, MNRAS, 423, 1109
Peñarrubia, J., Ma, Y.-Z., Walker, M. G., & McConnachie, A. 2014, MNRAS, 443, 2204
Pietrzyński, G., Gieren, W., Szewczyk, O., et al. 2008, AJ, 135, 1993
Pillepich, A., Nelson, D., Hernquist, L., et al. 2018, MNRAS, 475, 648
Radburn-Smith, D. J., de Jong, R. S., Streich, D., et al. 2014, ApJ, 780, 105
Read, J. I., Agertz, O., & Collins, M. L. M. 2016, MNRAS, 459, 2573
Read, J. I., & Erkal, D. 2019, MNRAS, 487, 5799
Read, J. I., Iorio, G., Agertz, O., & Fraternali, F. 2017, MNRAS, 467, 2019
Rekola, R., Jerjen, H., & Flynn, C. 2005, A&A, 437, 823
Richardson, J. C., Irwin, M. J., McConnachie, A. W., et al. 2011, ApJ, 732, 76
Rizzi, L., Held, E. V., Saviane, I., Tully, R. B., & Gullieuszik, M. 2007, MNRAS, 380, 1255
Sabbi, E., Calzetti, D., Ubeda, L., et al. 2018, ApJS, 235, 23
Samuel, J., Wetzel, A., Tollerud, E., et al. 2020, MNRAS, 491, 1471
Sanna, N., Bono, G., Stetson, P. B., et al. 2008, ApJL, 688, L69
Sarajedini, A., Yang, S. C., Monachesi, A., Lauer, T. R., & Trager, S. C. 2012, MNRAS, 425, 1459
Sawala, T., Frenk, C. S., Fattahi, A., et al. 2016a, MNRAS, 457, 1931
—. 2016b, MNRAS, 456, 85
Schaye, J., Crain, R. A., Bower, R. G., et al. 2015, MNRAS, 446, 521
Sharina, M. E., Karachentsev, I. D., & Tikhonov, N. A. 1999, Astronomy Letters, 25, 322

Sick, J., Courteau, S., Cuilland re, J.-C., et al. 2015, in IAU Symposium, Vol. 311, Galaxy Masses as Constraints of Formation Models, ed. M. Cappellari & S. Courteau, 82–85
Smercina, A., Bell, E. F., Price, P. A., et al. 2018, ApJ, 863, 152
Spencer, M., Loebman, S., & Yoachim, P. 2014, ApJ, 788, 146
Springel, V., Wang, J., Vogelsberger, M., et al. 2008, MNRAS, 391, 1685
Springel, V., Pakmor, R., Pillepich, A., et al. 2018, MNRAS, 475, 676
Stetson, P. B., Fiorentino, G., Bono, G., et al. 2014, PASP, 126, 616
Tanaka, M., Chiba, M., & Komiyama, Y. 2017, ApJ, 842, 127
Tikhonov, N. A., Lebedev, V. S., & Galazutdinova, O. A. 2015, Astronomy Letters, 41, 239
Tinker, J., Kravtsov, A. V., Klypin, A., et al. 2008, ApJ, 688, 709
Tollerud, E. J., Boylan-Kolchin, M., Barton, E. J., Bullock, J. S., & Trinh, C. Q. 2011, ApJ, 738, 102
Tonry, J. L., Dressler, A., Blakeslee, J. P., et al. 2001, ApJ, 546, 681
Trentham, N., & Tully, R. B. 2009, MNRAS, 398, 722
Vivas, A. K., & Mateo, M. 2013, AJ, 146, 141
Watkins, L. L., Evans, N. W., & An, J. H. 2010, MNRAS, 406, 264
Watkins, L. L., Evans, N. W., & van de Ven, G. 2013, MNRAS, 430, 971
Watkins, L. L., van der Marel, R. P., Sohn, S. T., & Evans, N. W. 2019, ApJ, 873, 118
Weisz, D. R., Dolphin, A. E., Martin, N. F., et al. 2019, MNRAS, 489, 763
Wetzel, A. R., Hopkins, P. F., Kim, J.-h., et al. 2016, ApJL, 827, L23
Wheeler, C., Hopkins, P. F., Pace, A. B., et al. 2019, MNRAS, 490, 4447
Woo, J., Courteau, S., & Dekel, A. 2008, MNRAS, 390, 1453
Woodley, K. A. 2006, AJ, 132, 2424
Yniguez, B., Garrison-Kimmel, S., Boylan-Kolchin, M., & Bullock, J. S. 2014, MNRAS, 439, 73
Zhang, D., Luo, Y., & Kang, X. 2019, MNRAS, 486, 2440
Zschaechner, L. K., Rand, R. J., Heald, G. H., Gentile, G., & Józsa, G. 2012, ApJ, 760, 37

Table 13. NGC 1023 Satellites

Name	RA	Dec	M_g	M_V	$g-i$	r_e
	deg	deg				pc
			Confirmed Satellites			
dw0233+3852	38.4286	38.8716	-11.7±0.27	-11.92±0.27	0.52±0.11	745.3±49.7
dw0235+3850	38.9763	38.8361	-13.27±0.15	-13.52±0.15	0.6±0.01	532.0±86.4
IC 239	39.1171	38.969	-19.4**	-19.7**	0.76**	9378.2**
dw0237+3855	39.3284	38.9328	-14.91±0.1	-15.23±0.1	0.81±0.02	967.3±96.5
dw0237+3836	39.414	38.6004	-11.86±0.17	-12.12±0.17	0.65±0.07	533.0±63.0
dw0239+3926	39.8318	39.435	-12.12±0.14	-12.42±0.14	0.75±0.02	1305.3±103.8
dw0239+3903	39.8451	39.0559	-9.02±0.49	-9.3±0.49	0.7±0.18	228.8±44.0
dw0239+3902	39.9476	39.0484	-9.46±0.09	-9.79±0.09	0.82±0.02	267.3±15.8
UGC 2157	40.1046	38.563	-16.1**	-16.4**	0.66**	1986.6**
dw0240+3854	40.1376	38.9004	-13.32±0.03	-13.49±0.03	0.42±0.01	330.2±3.3
dw0240+3903	40.1555	39.0554	-17.1**	-17.4**	0.76**	2045.7**
dw0240+3922	40.165	39.3791	-13.4±0.07	-13.51±0.07	0.26±0.01	644.2±53.4
dw0241+3904	40.2514	39.0721	-14.16±0.03	-14.34±0.03	0.42±0.01	781.8±25.9
UGC 2165	40.3148	38.7438	-15.88±0.04	-16.23±0.04	0.89±0.01	1261.0±40.3
dw0242+3838	40.6023	38.635	-9.24±0.11	-9.43±0.11	0.45±0.06	181.0±12.3
			Possible Satellites			
dw0238+3805	39.6712	38.085	-13.4**	-13.6**	0.57**	656.2**
dw0239+3910	39.842	39.1729	-7.74±0.24	-8.01±0.24	0.66±0.14	227.6±22.7
dw0241+3852	40.3364	38.8667	-8.73±0.42	-8.99±0.42	0.64±0.13	310.2±42.0
dw0241+3829	40.4759	38.4982	-10.6±0.13	-10.85±0.13	0.64±0.02	300.1±30.1
dw0242+3757	40.5923	37.9567	-7.4±0.19	-7.79±0.19	0.99±0.13	95.1±11.4
dw0243+3915	40.9792	39.2558	-11.13±0.13	-11.43±0.13	0.74±0.04	313.7±47.2

Note—Confirmed and possible satellites in the NGC 1023 system. The V band photometry is converted from our photometry, as described in Carlsten et al. (2019c). The asterisks mark systems which were not well fit by a Sérsic profile and the photometry might be somewhat biased.

APPENDIX

A. LV SATELLITE SYSTEMS

A.1. *Systems Surveyed In the Current Work*

Tables 13 - 21 list the properties of the confirmed and possible satellites in the systems that we have surveyed. Position, magnitudes, and sizes are given for all system members, including the hosts. The host photometry comes from Gil de Paz et al. (2007). For the satellites, the host distance is used to calculate absolute magnitudes and physical sizes and not the individual SBF distances. We are not able to resolve the 3D structure of these groups with the precision of SBF, and using the SBF distances would simply increase the scatter in size and magnitude.

In Carlsten et al. (2019c), R band photometry from Trentham & Tully (2009) was used for some of the largest candidates around NGC 1023. We convert from R into V using $V \approx R + 0.56$ (Fukugita et al. 1995). **redo the tables with this also put the host Mvs in as well**

A.2. *Previously Surveyed Systems*

Table 22 - 27 lists the members of the previously surveyed systems. Positions, distances, and luminosities are given for all satellites.

B. LUMINOSITY FUNCTION CHECKS WITH THE ELVIS SIMULATION SUITE

Figure 10 shows the analogous plot to Figure 6 for the ELVIS (Garrison-Kimmel et al. 2014) zoom DMO simu-

Table 14. NGC 1156 Satellites

Name	RA	Dec	M_g	M_V	$g-r$	r_e
	deg	deg				pc
Confirmed Satellites						
Possible Satellites						
dw0300+2514	45.0739	25.2485	-10.39±0.5	-10.58±0.5	0.33±0.11	213.7±31.0
dw0301+2446	45.3848	24.7827	-10.36±0.35	-10.69±0.37	0.57±0.21	387.7±49.8

Note—Confirmed and possible satellites in the NGC 1156 system.

Table 15. NGC 2903 Satellites

Name	RA	Dec	M_g	M_V	$g-r$	r_e
	deg	deg				pc
Confirmed Satellites						
dw0930+2143	142.6665	21.7244	-10.86±0.08	-11.0±0.09	0.24±0.03	297.6±21.5
UGC 5086	143.2036	21.4654	-13.79±0.08	-14.12±0.08	0.56±0.03	653.6±30.3
Possible Satellites						
dw0933+2114	143.3685	21.2334	-8.1±0.49	-8.42±0.49	0.54±0.1	186.7±24.1
dw0934+2204	143.592	22.0815	-10.14±0.13	-10.32±0.13	0.29±0.02	148.6±24.3

Note—Confirmed and possible satellites in the NGC 2903 system.

lation. The observed 'MW-sized' host satellite systems are compared with those predicted by the ELVIS DMO simulations combined with our fiducial SHMR. The thin black lines show the predicted LFs for the ELVIS hosts mock observed from a random direction and forward modelled through the survey area selection function for a specific host, as described in §9. For each of the 48 ELVIS hosts, 10 random directions are used.

The ELVIS LFs are noticeably richer in satellites than the LFs predicted by TNG using the same SHMR. As explained in the main text this is because the ELVIS hosts are, on average, more massive than the TNG 'MW-like' hosts. A secondary, smaller effect is that the ELVIS subhalos do not experience any disruption by a central disk while the TNG subhalos do.

C. HSC OBSERVATIONS OF NGC 4631

To confirm our SBF results for many of the candidates found around NGC 4631, we used the much deeper HSC data of Tanaka et al. (2017). The CFHT/Megacam data we used for this region had ~ 1 hour exposure times for most of the field. The HSC data, on the other hand, has ~ 10 hour exposure time (on a telescope with twice the aperture of CFHT). The CFHT data is wider field, however, so we find a few candidates that were outside of the footprint of Tanaka et al. (2017).

To use the HSC data, we downloaded the raw data from the Subaru archive[9] and reduced it using version 4 of the HSC pipeline (Bosch et al. 2018). For the sake of saving computing time, we only downloaded and stacked ~ 3 hours of g and i band data each. We then did a SBF analysis on cutouts for several of the candidates that are in the HSC footprint. Because the HSC pipeline does a very local (128×128 pixel grid) background estimation and subtraction, we did not attempt an SBF analysis for dw1240+3247 or dw1242+3237. These two dwarfs are large and very LSB (and also near NGC 4631 in projection), and the pipeline sky subtraction was clearly over-subtracting some diffuse light from these galaxies. This over-subtraction can have a significant effect on the SBF results, so we did not look at these dwarfs. To

[9] https://smoka.nao.ac.jp/fssearch.jsp

Table 16. NGC 4258 Satellites

Name	RA	Dec	M_g	M_V	$g-r$	r_e
	deg	deg				pc
			Confirmed Satellites			
NGC 4248	184.46	47.409	-16.57±0.02	-16.86±0.02	0.5±0.01	1824.1±17.1
LVJ1218+4655	184.5462	46.9169	-12.8±0.02	-12.93±0.02	0.22±0.01	564.8±20.4
dw1219+4743	184.7771	47.7308	-10.76±0.16	-10.99±0.16	0.4±0.04	361.4±43.8
UGC 7356	184.7879	47.0897	-14.0±0.09	-14.31±0.1	0.52±0.05	896.4±60.2
dw1220+4729	185.1279	47.4909	-9.16±0.35	-9.32±0.35	0.27±0.12	479.8±68.2
dw1220+4649	185.2287	46.8304	-10.47±0.13	-10.76±0.14	0.49±0.05	402.9±23.6
dw1223+4739	185.9428	47.6589	-11.27±0.09	-11.53±0.09	0.45±0.04	601.6±80.9
			Possible Satellites			
dw1218+4623	184.5111	46.3846	-9.29±0.44	-9.55±0.44	0.43±0.09	649.3±111.3
dw1220+4922	185.0597	49.3809	-9.29±0.04	-9.47±0.05	0.29±0.06	169.0±7.8
dw1220+4748	185.2326	47.8164	-7.31±0.38	-7.52±0.39	0.36±0.13	159.2±32.2
dw1223+4848	185.8031	48.8156	-8.39±0.22	-8.7±0.22	0.54±0.07	164.1±21.7

Note—Confirmed and possible satellites in the NGC 4258 system.

turn the measured SBF magnitudes into distances, we used the i band calibration of Carlsten et al. (2019b). As our goal is mostly just to confirm the CFHT results, we do not bother with any filter conversions to convert the CFHT/Megacam calibration into the HSC filter system. Both filter systems are based on SDSS filters so they should not differ by much. We assume a 0.1 mag uncertainty in the $g-i$ color of each galaxy.

Table 28 gives the SBF results for the HSC data. The results are remarkably consistent with what we found with the CFHT data. One surprising result from §5.6 was that several of the dSph candidates found around NGC 4631 were actually background. These objects are prototypical dSphs and were very clustered around NGC 4631. There does not appear to be an obvious possible massive host for these objects behind NGC 4631, so this result was surprising. The HSC data confirms that dw1243+3228, dw1240+3239, and dw1242+3227 are all background. In §5.6, the SBF results were ambiguous for dw1242+3227 given its extreme faintness, but with the HSC data, it is clearly background. For the remaining objects, the HSC data confirms them to be at the distance of NGC 4631 with *much* higher S/N than was possible with the CFHT data.

The consistency between the HSC results and the shallower CFHT results gives us confidence in the distance constraints we derive for candidates around other hosts in the CFHT data. This also gives a taste of what is possible for SBF with 8m class telescopes, in particular with LSST.

D. r-BAND SBF CALIBRATION

In Figure 11 we show the conversions between $\bar{M}_r$ and $\bar{M}_r$ and $g-i$ and $g-r$ that we use to derive the r-band calibration used in this work. The color-color transformation has quite low scatter. The SBF magnitude transformation looks significantly worse but we note that the galaxies we analyze in this paper all have $g-r \lesssim 0.6$ where the scatter is more reasonable. Additionally, an error of 0.1 mag in the conversion between i and r band SBF magnitudes will only introduce a 5% error in distance which is less than the usual distance uncertainties we find in the SBF analysis. While a quadratic looks to be more appropriate for the SBF magnitude conversion, using a linear fit has the attractive property that the $\bar{M}_r$ versus $g-r$ relation will be linear as well.

E. EXAMPLES OF CONFIRMED SATELLITES, BACKGROUND CONTAMINANTS, AND UNCONFIRMED CANDIDATES

Figure 12 shows examples of galaxies that we conclude to be background along with examples of galaxies that we conclude to be real satellites from the same host. The galaxies that we constrain to be background are roughly the same surface brightness as the confirmed satellites but show visibly smoother surface brightness profiles without any SBF. The example background galaxy from the NGC 4258 region (dw1219+4705) was confirmed to

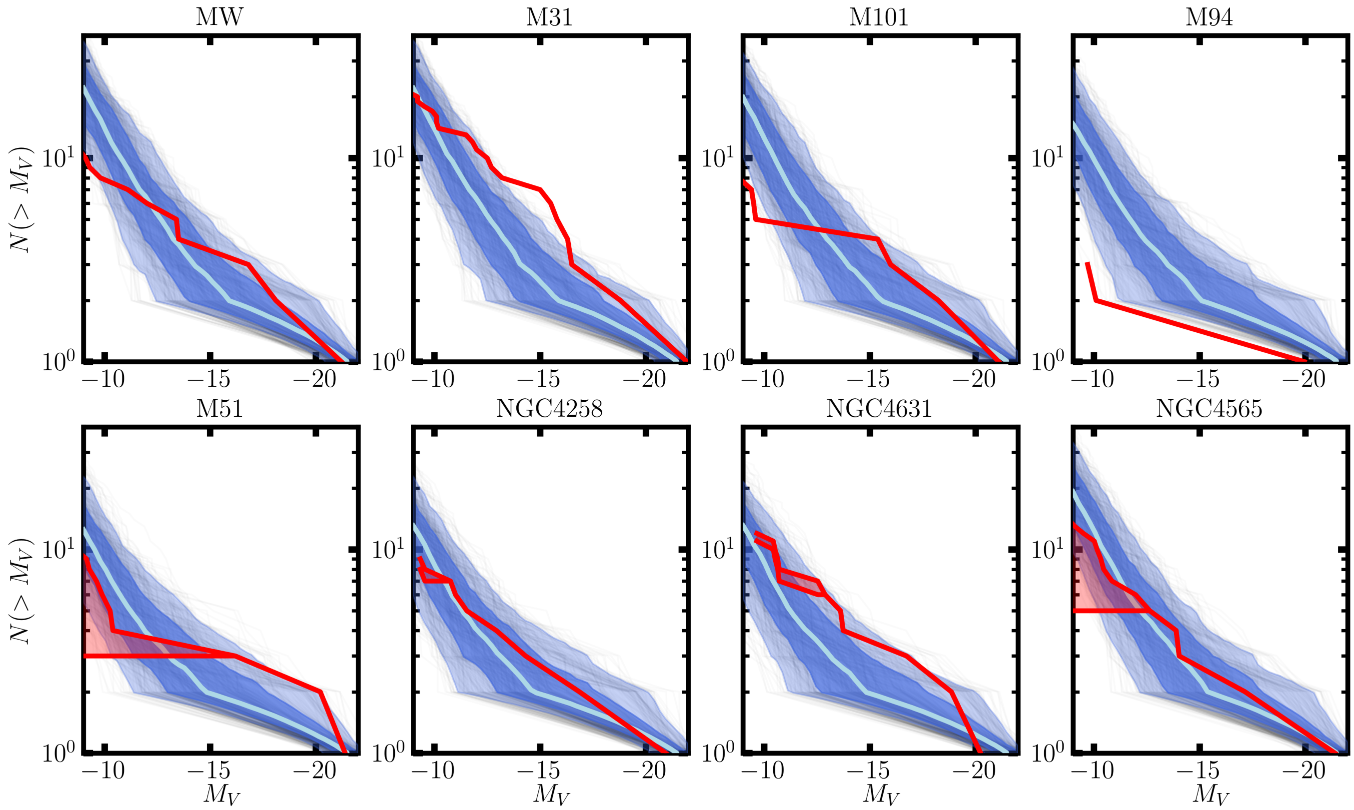

Figure 10. The cumulative luminosity functions for the 8 'MW-sized' hosts that have been well surveyed for satellites (red). The thin black lines show the predicted LFs from the abundance matching model described in the text combined with the ELVIS zoom DMO simulation. The blue regions show the $\pm 1, 2\sigma$ spread in the models. The luminosity completeness is different for each host but is $M_V \lesssim -9$ in all cases. For each host, the model satellite systems have been forward modeled considering the survey area selection function for that specific host.

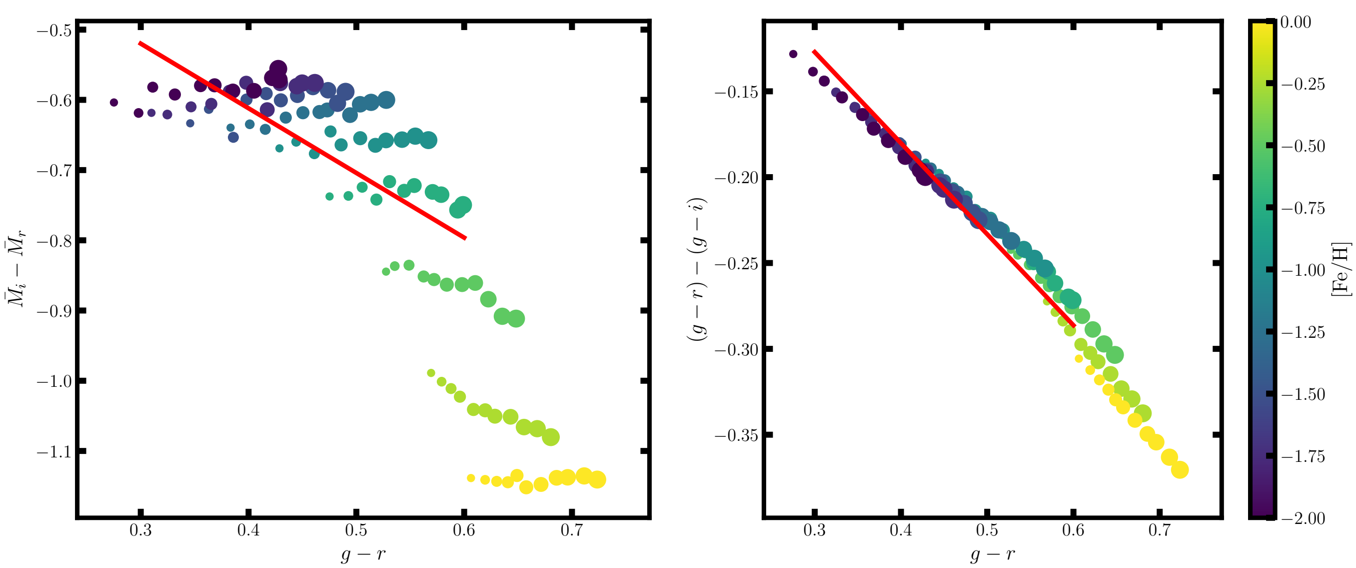

Figure 11. The filter conversions used in deriving the r-band calibration. The points show the SSP models where point size represents age ($3 <$ age < 10 Gyr) with biggest sizes indicating oldest ages. The red lines show the fits that are used in the conversion.

Table 17. NGC 4565 Satellites

Name	RA	Dec	M_g	M_V	$g-r$	r_e
	deg	deg				pc
			Confirmed Satellites			
dw1234+2531	188.5971	25.5193	-13.73±0.03	-14.03±0.03	0.5±0.01	1148.5±28.2
NGC 4562	188.8977	25.852	-16.88±0.01	-17.14±0.01	0.45±0.01	2043.7±8.0
IC 3571	189.0836	26.084	-13.8**	-13.9**	0.15**	491.1**
dw1237+2602	189.2551	26.0357	-12.41±0.06	-12.64±0.06	0.38±0.01	484.5±33.6
			Possible Satellites			
dw1233+2535	188.2961	25.5987	-11.73±0.07	-11.96±0.07	0.4±0.01	269.3±11.5
dw1233+2543	188.3267	25.7263	-9.81±0.1	-10.01±0.1	0.34±0.03	238.9±11.6
dw1234+2627	188.6042	26.4542	-8.53±0.26	-8.8±0.26	0.46±0.09	212.4±33.1
dw1234+2618	188.7399	26.314	-10.13±0.06	-10.32±0.06	0.32±0.03	267.8±10.0
dw1235+2616	188.8438	26.2717	-9.84±0.13	-10.14±0.13	0.51±0.03	259.1±51.5
dw1235+2534	188.9066	25.5702	-8.45±0.21	-8.65±0.22	0.36±0.09	246.2±45.2
dw1235+2637	188.9252	26.6208	-8.7±0.31	-8.73±0.34	0.06±0.25	387.9±97.8
dw1235+2609	188.9799	26.1654	-7.64±0.21	-7.87±0.22	0.39±0.08	172.8±30.7
dw1235+2606	188.9853	26.1153	-11.32±0.3	-11.37±0.31	0.09±0.16	1589.2±236.8
dw1236+2616	189.0247	26.2735	-7.5±0.15	-7.78±0.16	0.48±0.06	172.4±10.8
dw1236+2603	189.1049	26.0552	-8.93±0.19	-9.09±0.2	0.28±0.07	258.2±41.7
dw1236+2634	189.2448	26.5782	-9.2±0.18	-9.5±0.18	0.5±0.04	272.2±29.8
dw1237+2605	189.3614	26.0855	-10.6±0.32	-10.85±0.32	0.41±0.07	761.0±194.6
dw1237+2637	189.4278	26.6253	-10.15±0.08	-10.45±0.08	0.52±0.06	281.9±32.5
dw1237+2631	189.4777	26.5188	-7.86±0.36	-8.12±0.37	0.43±0.09	155.6±18.6
dw1238+2610	189.6651	26.1669	-8.39±0.29	-8.65±0.29	0.44±0.09	270.7±29.1

Note—Confirmed and possible satellites in the NGC 4565 system.

Table 18. NGC 4631 Satellites

Name	RA	Dec	M_g	M_V	$g-r$	r_e
	deg	deg				pc
			Confirmed Satellites			
dw1239+3230	189.7705	32.5043	-10.26±0.09	-10.43±0.09	0.29±0.03	286.8±18.0
dw1239+3251	189.8318	32.8612	-9.31±0.31	-9.65±0.31	0.58±0.11	490.4±98.9
dw1240+3216	190.2209	32.282	-10.35±0.1	-10.64±0.1	0.49±0.05	311.5±20.0
dw1240+3247	190.2451	32.7897	-13.28±0.64	-13.61±0.67	0.57±0.33	2549.6±684.5
dw1241+3251	190.4463	32.8573	-13.65±0.05	-13.73±0.05	0.13±0.02	644.4±33.3
NGC 4627	190.4985	32.5739	-16.5**	-16.7**	0.36**	973.9**
dw1242+3237	190.5256	32.6203	-10.47±0.43	-10.7±0.44	0.4±0.17	660.6±99.1
dw1242+3158	190.6309	31.9693	-10.22±0.1	-10.51±0.1	0.49±0.05	295.2±22.0
dw1243+3228	190.8537	32.4819	-12.62±0.03	-12.88±0.03	0.44±0.01	593.9±10.7
			Possible Satellites			
dw1242+3231	190.6184	32.5308	-12.28±0.18	-12.53±0.18	0.42±0.01	402.7±63.7

NOTE—Confirmed and possible satellites in the NGC 4631 system.

Table 19. NGC 5023 Satellites

Name	RA	Dec	M_g	M_V	$g-i$	r_e
	deg	deg				pc
			Confirmed Satellites			
			Possible Satellites			
dw1314+4420	198.6437	44.3341	-6.67±0.16	-6.91±0.18	0.58±0.18	96.4±8.2

NOTE—Confirmed and possible satellites in the NGC 5023 system.

be background by Cohen et al. (2018) as well. The galaxy pairs in Figure 12 are only roughly matched in color so color could play a role in their different appearances, but color *is* taken into account in the quantitative SBF analysis.

Figure 13 shows an example dwarf that is too LSB to be confirmed as either a satellite or background contaminant with the current data.

Table 20. M51 Satellites

Name	RA	Dec	M_g	M_V	$g-r$	r_e
	deg	deg				pc
			Confirmed Satellites			
NGC 5195	202.4696	47.1952	-20.2**	-20.2**	0.0**	0.0**
NGC 5229	203.5127	47.9124	-15.95±0.01	-16.18±0.01	0.4±0.01	1543.2±3.9
			Possible Satellites			
dw1327+4637	201.7945	46.6323	-8.3±0.24	-8.64±0.24	0.57±0.11	195.6±42.7
dw1327+4626	201.9725	46.4406	-8.92±0.2	-9.14±0.2	0.38±0.03	163.6±31.7
dw1328+4703	202.1027	47.0649	-9.27±0.11	-9.62±0.11	0.59±0.04	279.9±17.5
dw1330+4731	202.6405	47.5264	-9.67±0.15	-9.89±0.16	0.37±0.11	519.0±50.8
dw1331+4654	202.7839	46.9076	-7.45±0.08	-7.77±0.1	0.55±0.08	129.4±4.1
dw1331+4648	202.7983	46.8158	-9.02±0.17	-9.28±0.17	0.44±0.03	286.4±44.6

Note—Confirmed and possible satellites in the M51 system.

Table 21. M104 Satellites

Name	RA	Dec	M_g	M_V	$g-i$	r_e
	deg	deg				pc
Confirmed Satellites						
dw1237-1125	189.2986	-11.4331	-11.62±0.06	-12.02±0.1	0.99±0.23	463.5±17.9
dw1239-1159	189.7866	-11.9876	-11.0±0.22	-11.21±0.22	0.52±0.08	653.8±117.3
dw1239-1152	189.7881	-11.8763	-8.09±0.22	-8.29±0.23	0.49±0.1	229.0±33.4
dw1239-1143	189.8136	-11.7189	-13.38±0.03	-13.7±0.03	0.8±0.01	577.7±11.9
dw1239-1113	189.8851	-11.2253	-11.9±0.27	-12.23±0.27	0.84±0.13	799.9±119.3
dw1239-1120	189.9628	-11.342	-10.49±0.1	-10.73±0.1	0.59±0.03	323.2±29.2
dw1239-1144	189.9839	-11.7479	-12.57±0.29	-12.85±0.3	0.7±0.14	1039.4±208.2
dw1240-1118	190.0351	-11.309	-14.0±0.03	-14.32±0.03	0.81±0.01	697.1±16.9
dw1240-1140	190.0737	-11.679	-10.64±0.46	-11.01±0.46	0.94±0.06	606.6±130.9
dw1241-1131	190.2617	-11.5289	-10.12±0.17	-10.44±0.18	0.8±0.11	423.3±40.8
dw1241-1153	190.3006	-11.8915	-11.57±0.22	-11.86±0.22	0.72±0.06	706.4±104.5
dw1241-1155	190.3298	-11.9318	-12.42±0.11	-12.72±0.11	0.75±0.06	786.1±54.6
Possible Satellites						
dw1238-1208	189.5927	-12.1357	-7.27±0.15	-7.52±0.21	0.61±0.37	155.8±10.0
dw1238-1116	189.6297	-11.2735	-8.83±0.34	-9.0±0.35	0.4±0.2	270.6±51.3
dw1238-1122	189.64	-11.368	-13.4**	-13.8**	0.89**	1605.0**
dw1238-1102	189.7429	-11.0361	-9.17±0.25	-9.38±0.26	0.5±0.16	241.1±26.1
dw1239-1154	189.843	-11.907	-8.47±0.45	-8.76±0.46	0.73±0.18	386.1±60.9
dw1239-1118	189.9059	-11.309	-8.31±0.13	-8.54±0.14	0.58±0.1	184.3±18.5
dw1239-1106	189.9242	-11.1006	-9.02±0.18	-9.27±0.19	0.61±0.09	272.7±39.9
dw1241-1123	190.2895	-11.3989	-8.82±0.38	-9.14±0.38	0.8±0.09	565.5±116.6
dw1241-1105	190.2927	-11.0973	-8.01±0.11	-8.4±0.11	0.99±0.06	107.0±10.7
dw1242-1116	190.6826	-11.2745	-11.81±0.22	-12.05±0.22	0.58±0.07	1127.6±213.2
dw1242-1129	190.7067	-11.4894	-8.82±0.23	-9.11±0.24	0.73±0.13	150.5±22.3
dw1243-1137	190.8249	-11.6257	-8.34±0.19	-8.75±0.2	1.03±0.07	203.7±36.1

Note—Confirmed and possible satellites in the M104 system.

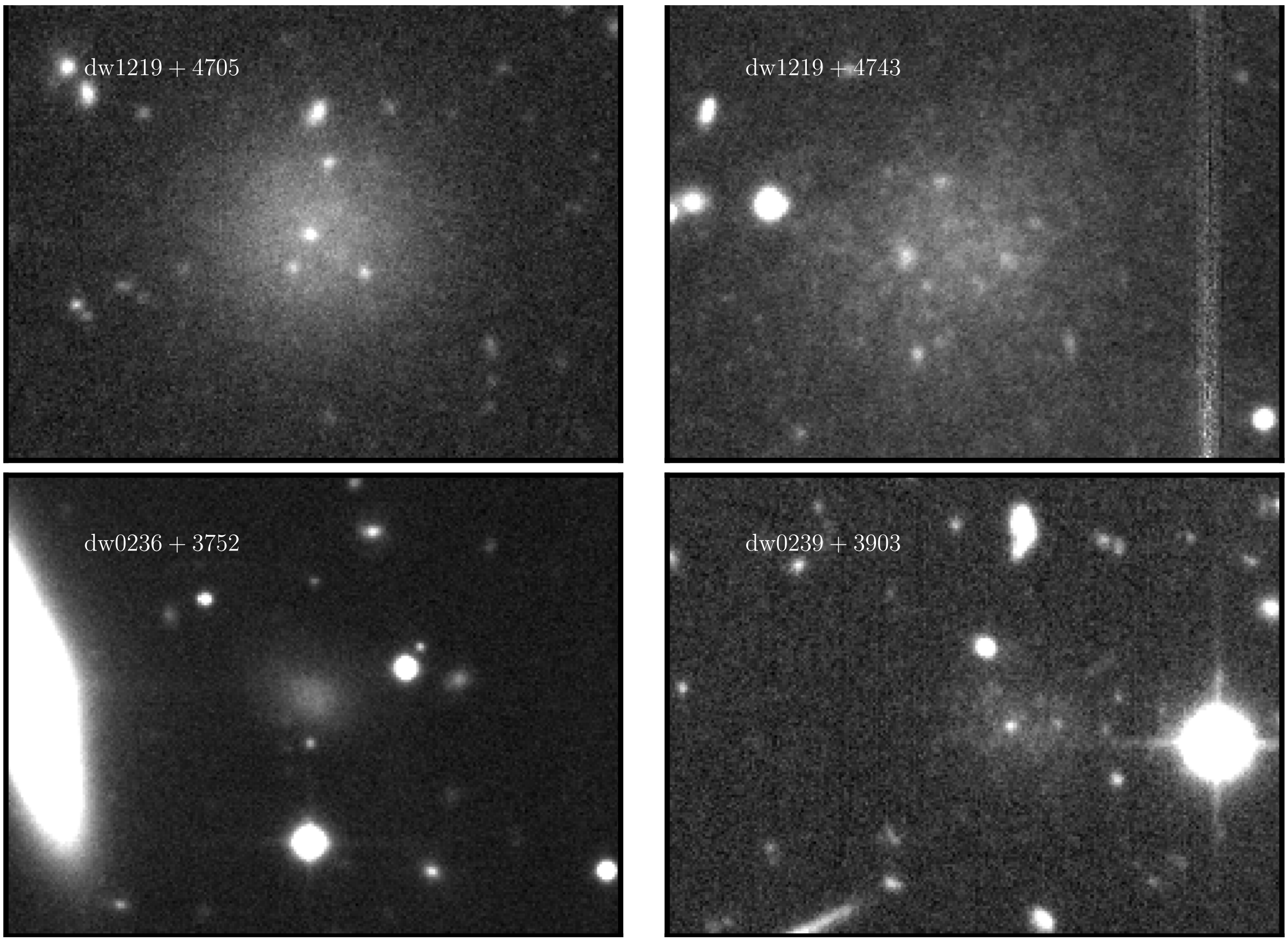

Figure 12. The left column shows examples of galaxies that we constrain to be background in the SBF analysis and the right column shows examples of confirmed satellites. The top row galaxies are from the NGC 4258 region and the bottom row are from NGC 1023. The real satellites exhibit clearly visible SBF while the background galaxies are nearly perfectly smooth. The pairs of galaxies from each region are roughly matched in surface brightness, size, and color?. Each image is 45″ wide. Top row is r band and the bottom row is i.

Table 22. MW Satellites

M81, $M_* = 5 \times 10^{10} M_\odot$					
Name	RA deg	Dec deg	$D_\odot$ kpc	M_V	Source
MW	–	–	–	-21.2	–
LMC	05:23:34	-69:45:22	51	-18.1	1,1,1
SMC	00:52:44	-72:49:43	64	-16.8	1,1,1
Sgr	18:55:19	-30:32:43	27	-13.6	1,2,1
Fornax	02:39:59	-34:26:57	139	-13.3	1,3,1
Leo 1	10:08:28	+12:18:23	269	-12.1	1,4,1
Sculptor	01:00:09	-33:42:33	85	-11.1	1,5,1
Leo 2	11:13:28	+22:09:06	225	-9.7	1,6,1
Sextans	10:13:03	-01:36:53	86	-9.3	1,7,1
Ursa Minor	15:09:08	+67:13:21	76	-8.8	1,8,1
Carina	06:41:36	-50:57:58	104	-9.1	1,9,1
Draco	17:20:12	+57:54:55	79	-8.9	1,10,1
CVn 1	13:28:03	+33:33:21	211	-8.5	1,11,1

NOTE—Known satellites of the MW. Sources for position, distance, and luminosity (in order): sources 1-McConnachie (2012), 2-Hamanowicz et al. (2016), 3-Rizzi et al. (2007), 4-Stetson et al. (2014), 5-Martínez-Vázquez et al. (2016); Pietrzyński et al. (2008), 6-Bellazzini et al. (2005); Gullieuszik et al. (2008), 7-Mateo et al. (1995), 8-Carrera et al. (2002); Bellazzini et al. (2002), 9-Coppola et al. (2015); Vivas & Mateo (2013), 10-Bonanos et al. (2004); Kinemuchi et al. (2008), 11-Kuehn et al. (2008)

Figure 13. An example of a dwarf (dw1218+4623) that was too LSB to be either confirmed as a satellite or constrained to be background.

Table 23. M31 Satellites

M31, $M_* = 10.3 \times 10^{10} M_\odot$					
Name	RA deg	Dec deg	$D_\odot$ Mpc	M_V	Source
M31	00:42:44	+41:16:09	0.780	-21.95	1,2,3
M33	01:33:50	+30:39:37	0.821	-18.8	1,2,1
NGC 205	00:40:22	+41:41:07	0.824±0.027	-16.5	1,4,1
M32	00:42:41	+40:51:55	0.781±0.02	-16.3	1,5,1
NGC 147	00:33:12	+48:30:32	0.713	-15.8	1,2,1
IC 10	00:20:17	+59:18:14	0.798±0.029	-15.0	1,6,1
NGC 185	00:38:58	+48:20:15	0.619	-15.5	1,2,1
AndVII	23:26:31	+50:40:33	0.763±0.035	-13.2	1,4,1
AndXXXII	00:35:59.4	+51:33:35	$0.871^{0.018}_{0.016}$	-12.5	1,8,1
AndII	01:16:29.8	+33:25:09	0.679±0.040	-12.7	1,9,1
AndI	00:45:39.8	+38:02:28	0.791±0.050	-12.0	1,9,1
AndXXXI	22:58:16.3	+41:17:28	$0.794^{0.018}_{0.013}$	-11.8	1,8,1
AndIII	00:35:33.8	+36:29:52	0.745±0.039	-10.2	1,9,1
AndXXIII	01:29:21.8	+38:43:8	$0.809^{0.022}_{0.01}$	-9.9	1,8,1
AndVI	23:51:46.3	+24:34:57	0.783±0.025	-11.5	1,4,1
AndXXI	23:54:47.7	+42:28:15	$0.851^{0.019}_{0.011}$	-9.2	1,8,1
AndXXV	00:30:8.9	+46:51:7	$0.832^{0.021}_{0.015}$	-9.2	1,8,1
LGS3	01:3:55.0	+21:53:6	0.769±0.023	-10.1	1,4,1
AndXV	01:14:18.7	+38:7:3	0.766±0.042	-8.4	1,9,1
AndV	01:10:17.1	+47:37:41	0.774±0.028	-9.5	1,4,1
AndXIX	00:19:32.1	+35:2:37	0.805	-10.1	1,2,1
AndXIV	00:51:35.0	+29:41:49	$0.847^{0.021}_{0.015}$	-8.8	1,8,1
AndXVII	00:37:7.0	+44:19:20	$0.866^{0.025}_{0.013}$	-8.1	1,8,1
AndXXIX	23:58:55.6	+30:45:20	$0.820^{0.017}_{0.015}$	-8.5	1,8,1
AndIX	00:52:53.0	+43:11:45	$0.769^{0.021}_{0.012}$	-8.8	1,8,1
AndXXX	00:36:34.9	+49:38:48	$0.628^{0.016}_{0.015}$	-8.	1,8,1
AndXXVII	00:37:27.1	+45:23:13	0.827±0.047	-7.9	1,7,1
AndXXIV	01:18:30.0	+46:21:58	$0.724^{0.099}_{0.081}$	-8.0	1,8,1
AndX	01:6:33.7	+44:48:16	$0.711^{0.042}_{0.032}$	-7.5	1,8,1
AndXXVI	00:23:45.6	+47:54:58	$0.887^{0.089}_{0.077}$	-6.2	1,8,1
AndXI	00:46:20.0	+33:48:5	0.726	-6.3	1,2,1
AndXXII	01:27:40.0	+28:5:25	$0.929^{0.123}_{0.099}$	-6.8	1,8,1
AndXX	00:7:30.7	+35:7:56	$0.867^{0.044}_{0.034}$	-6.7	1,8,1
AndXIII	00:51:51.0	+33:0:16	0.740	-6.5	1,2,1
AndXII	00:47:27.0	+34:22:29	0.870	-7.0	1,2,1
AndXVI	00:59:29.8	+32:22:36	0.550±0.031	-7.6	1,9,1
AndXXXIII	03:1:23.6	+40:59:18	$0.755^{0.018}_{0.009}$	-10.2	1,8,1
AndXXVIII	22:32:41.2	+31:12:58	0.769±0.038	-8.8	1,9,1
AndXVIII	00:2:14.5	+45:5:20	$1.219^{0.029}_{0.013}$	-9.2	1,8,1

NOTE—Known satellites of the M31. For the distances without errorbars, Conn et al. (2012) provides the entire distance posterior which is what is used. For these cases, the median distance is reported. Sources for position, distance, and luminosity (in order): 1-McConnachie et al. (2018), 2-Conn et al. (2012), 3-Sick et al. (2015), 4-McConnachie et al. (2005), 5-Watkins et al. (2013); Tonry et al. (2001); Jensen et al. (2003); Monachesi et al. (2011); Sarajedini et al. (2012); Fiorentino et al. (2012), 6-Sanna et al. (2008), 7-Richardson et al. (2011), 8-Weisz et al. (2019), 9-Martínez-Vázquez et al. (2017),

Table 24. M81 Satellites

M81, $M_* = 5 \times 10^{10} M_\odot$					
Name	RA	Dec	$D_\odot$	M_V	Source
	deg	deg	Mpc		
M81	09:55:33.2	+69:03:55	3.69	-21.1	1,3,2
M82	09:55:52.4	+69:40:47	3.61	-19.75	1,3,2
NGC 3077	10:03:19.1	+68:44:02	3.82	-17.93	1,3,2
NGC 2976	09:47:15.5	+67:54:59	3.66	-17.83	1,3,2
IC 2574	10:28:23.6	+68:24:43	3.93	-17.19	1,3,2
DDO 82	10:30:36.58	+70:37:06	3.93	-15.06	1,3,2
KDG 61	9:57:02.7	+68:35:30	3.66	-13.4	1,3,4
BK5N	10:04:40.3	+68:15:20	3.70	-11.23	1,3,4
IKN	10:08:05.9	+68:23:57	3.75	-14.3	1,3,4
FM1	9:45:10.0	+68:45:54	3.78	-11.3	1,3,1
KDG 64	10:07:01.9	+67:49:39	3.75	-13.3	1,3,4
F8D1	09:44:47.1	+67:26:19	3.75	-12.8	1,3,1
d0944p69	09:44:22.5	+69:12:40	3.84	-6.4	1,3,1
d1014p68	10:14:55.8	+68:45:27	3.84	-9.0	1,3,1
KK77	9:50:10.0	+67:30:24	3.80	-12.6	1,3,1
d1006p67	10:06:46.2	+67:12:04	3.61	-9.4	1,3,1
d0939p71	09:39:15.9	+71:18:42	3.65	-9.0	1,3,1
KDG 63	10:05:07.3	+66:33:18	3.65	-12.6	1,3,1
d0958p66	09:58:48.5	+66:50:59	3.82	-12.8	1,3,1
ddo78	10:26:27.9	+67:39:24	3.48	-12.4	1,3,1
d1028p70	10:28:39.7	+70:14:01	3.84	-12.0	1,3,1
d1015p69	10:15:06.9	+69:02:15	4.07	-8.4	1,3,1
d0955p70	09:55:13.6	+70:24:29	3.45	-9.4	1,3,1
d1041p70	10:41:16.8	+70:09:03	3.70	-8.9	1,3,1
HS117	10:21:25.2	+71:06:58	3.96	-11.7	1,3,1
d0944p71	09:44:34.4	+71:28:57	3.47	-12	1,3,1
d1012p64	10:12:48.4	+64:06:27	3.7	-12.9	1,3,1
d0926p70	09:26:27.9	+70:30:24	3.4	-9.4	1,3,1
Ho1	09:40:32.3	+71:11:11	4.02	-14.2	1,3,1
BK6N	10:34:31.9	+66:00:42	3.31	-11.3	1,3,1
d0934p70	09:34:03.7	+70:12:57	3.02	-9.0	1,3,1

Note—Known satellites of M81. Sources for position, distance, and luminosity (in order): 1-Chiboucas et al. (2013), 2-Gil de Paz et al. (2007), 3-Karachentsev et al. (2013), 4-Okamoto et al. (2019)

Table 25. CenA Satellites

CenA, $M_* = 8 \times 10^{10} M_\odot$					
Name	RA	Dec	$D_\odot$	M_V	Source
	deg	deg	Mpc		
CenA	13:25:27.6	-43:01:09	3.77	-21.04	1,1,1
KK189	198.1875	-41.8319	4.23	-11.2	1,1,1
ESO269-066	198.2875	-44.8900	3.75	-14.1	1,1,1
NGC 5011C	198.2958	-43.2656	3.73	-13.9	1,1,1
CenA-Dw11	199.4550	-42.9269	3.52 ± 0.35	-9.4	2,2,2
CenA-Dw5	199.9667	-41.9936	3.61 ± 0.33	-8.2	2,2,2
KK196	200.4458	-45.0633	3.96	-12.5	1,1,1
KK197	200.5042	-42.5356	3.84	-12.6	1,1,1
KKs55	200.5500	-42.7308	3.85	-12.4	1,1,1
CenA-Dw10	200.6214	-39.8839	3.27 ± 0.44	-7.8	2,2,2
dw1322-39	200.6558	-39.9084	2.95 ± 0.05	-10.0	1,1,1
CenA-Dw4	200.7583	-41.7861	4.09 ± 0.26	-9.9	2,2,2
dw1323-40b	201.0000	-40.8367	3.91 ± 0.6	-9.9	1,1,1
dw1323-40	201.2421	-40.7622	3.73 ± 0.15	-10.4	1,1,1
CenA-Dw6	201.4875	-41.0942	4.04 ± 0.20	-9.1	2,2,2
CenA-Dw7	201.6167	-43.5567	4.11 ± 0.27	-9.9	2,2,2
ESO324-024	201.9042	-41.4806	3.78	-15.5	1,1,1
KK203	201.8667	-45.3525	3.78	-10.5	1,1,1
dw1329-45	202.3121	-45.1767	2.90 ± 0.12	-8.4	1,1,1
CenA-Dw2	202.4875	-41.8731	4.14 ± 0.23	-9.7	2,2,2
CenA-Dw1	202.5583	-41.8933	3.91 ± 0.12	-13.8	2,2,2
CenA-Dw3	202.5875	-42.19255	3.88 ± 0.16	-13.1	2,2,2
CenA-Dw9	203.2542	-42.5300	3.81 ± 0.36	-9.1	2,2,2
CenA-Dw8	203.3917	-41.6078	3.47 ± 0.33	-9.7	2,2,2
dw1336-44	204.2033	-43.8578	3.50 ± 0.28	-8.6	1,1,1
NGC5237	204.4083	-42.8475	3.33	-15.3	1,1,1
KKs57	205.4083	-42.5819	3.83	-10.6	1,1,1
dw1341-43	205.4221	-44.4485	3.53 ± 0.02	-10.1	1,1,1
dw1342-43	205.7029	-43.8561	2.90 ± 0.14	-9.8	1,1,1
KK213	205.8958	-43.7692	3.77	-10.0	1,1,1

Note—Known satellites of CenA. Sources for position, distance, and luminosity (in order): 1-Müller et al. (2019), 2-Crnojević et al. (2019)

Table 26. M101 Satellites

M101, $M_* = 4 \times 10^{10} M_\odot$					
Name	RA	Dec	$D_\odot$	M_V	Source
	deg	deg	Mpc		
M101	14:03:12.5	+54:20:56	6.52 ± 0.19	-21.1	1,3,1
NGC 5474	14:05:01.6	+53:39:44	6.82 ± 0.41	-18.24	1,1,1
NGC 5477	14:05:33.3	+54:27:40	6.77 ± 0.40	-15.37	1,1,1
HolmIV	13:54:45.7	+53:54:03	6.93 ± 0.48	-15.98	1,1,1
DF1	14:03:45.0	+53:56:40	6.37 ± 0.35	-9.6	5,5,5
DF2	14:08:37.5	+54:19:31	6.87 ± 0.26	-9.4	5,5,5
DF3	14:03:05.7	+53:36:56	6.52 ± 0.26	-8.8	5,5,5
dwa	14:06:49.9	+53:44:30	6.83 ± 0.27	-9.5	2,4,4
dw9	13:55:44.8	+55:08:46	7.34 ± 0.38	-8.2	2,4,4

Note—Known satellites of M101. Sources for position, distance, and luminosity (in order): 1-Tikhonov et al. (2015), 2-Bennet et al. (2017), 3-Beaton et al. (2019), 4-Bennet et al. (2019), 5-Danieli et al. (2017)

Table 27. M94 Satellites

M94, $M_* = 3 \times 10^{10} M_\odot$					
Name	RA	Dec	$D_\odot$	M_V	Source
	deg	deg	Mpc		
M94	12:50:53.1	+41:07:13	4.2	-19.95	1,1,2
dw1	12:55:02.5	40:35:22	4.1 ± 0.2	-10.1	3,3,3
dw2	12:51:04.4	41:38:10	4.7 ± 0.3	-9.7	3,3,3

Note—Known satellites of M94. Sources for position, distance, and luminosity (in order): 1-Karachentsev et al. (2013), 2-Gil de Paz et al. (2007), 3-Smercina et al. (2018)

Table 28. NGC 4631 SBF Results using HSC

Name	SBF S/N	Dist (Mpc)
dw1242+3227, HSC-1	3.7	> 10.4
dw1243+3232, HSC-5	10	> 11.0
dw1243+3228, HSC-6	18	6.6 ± 0.8
dw1240+3239, HSC-7	21	> 8.6
dw1241+3251, HSC-8	57	7.0 ± 0.8
dw1240+3216, HSC-9	21	7.4 ± 0.9
dw1242+3158, HSC-10	17	7.0 ± 0.8

Note—SBF results for candidates around NGC 4631 ($D = 7.4$ Mpc), using the extremely deep HSC data of Tanaka et al. (2017). For the distance lower bounds, 2σ lower bounds are given. For the distances, $\pm 1\sigma$ uncertainties are given.